Journal of Asian Earth Sciences 303 (2026) 107049

Contents lists available at ScienceDirect

Journal of Asian Earth Sciences

journal homepage: www.elsevier.com/locate/jseaes

Tectono-magmatic evolution of the central Kohistan Arc, NW Pakistan: Granitoid emplacement revealed by mineral chemistry☆

Tanveer Ahmad [a,*], Kirsten Drüppel [a], M.Qasim Jan [b,c], Armin Zeh [a], Dominik C. Hezel [d]

[a] *Institute of Applied Geosciences – Mineralogy and Petrology, Karlsruhe Institute of Technology (KIT), Adenauerring 20b, 76131 Karlsruhe, Germany*
[b] *National Centre of Excellence in Geology, University of Peshawar, Pakistan*
[c] *China-Pakistan Joint Research Centre (CPJRC) on Earth Sciences, Islamabad, Pakistan*
[d] *Institut Für Geowissenschaften, Goethe-Universität Frankfurt Am Main, Altenhöferallee 1, 60438 Frankfurt am Main, Germany*

ARTICLE INFO

Keywords:
Arc-continental collision
Assimilation
Central Kohistan Arc
Granitoids
Tectono-magmatic evolution

ABSTRACT

The central Kohistan Arc consists of Late Cretaceous to Early Tertiary, subduction-related, calc-alkaline to high-K granitoids with varied textures and compositions, reflecting several stages of a complex tectono-magmatic evolution. In this study, we present major elements data of amphibole, feldspar, and biotite, along with trace elements data of zircon from seven plutons, previously grouped into two categories: (1) pre-50 Ma intra-arc subduction-related and (2) post-50 Ma arc-continent collision-related granitoids. Amphibole compositions indicate that the intra-arc-related Late Cretaceous to Paleocene granitoids (Matiltan granite and Gabral quartz diorite) were less hydrous (~4.6–5.8 wt% H_2O) and crystallized at lower temperatures (740–745 °C) and pressures (3.0–3.6 kbar) corresponding to shallow mid-crustal depth, with oxygen fugacity of (logfO2: −17 to −15). The latter, Early Eocene (53 Ma) Deshai quartz diorites, which represents transitional magmatism between the waning intra-arc subduction phase and the onset of arc-continental collision, and the collision related Mid-Eocene (46–44 Ma) Diwanger, Shahibagh, and Jut Banda granitoids crystallized at relatively higher temperatures (774–785 °C) and pressures (3.7–4.5 kbar), indicating emplacement level in the deep mid crust as well as record oxygen fugacity of logfO2 = −14 to −13, and H_2O contents of 5.7–7.2 wt%. The biotite and zircon compositions consistently reflect a calc-alkaline subduction-related origin for all plutons. Zircon Eu-anomalies additionally suggest a progressive deepening of the magma sources from ca. 40 to 65 km depth, consistent with a change of the tectonic regime from arc-related to collision-related magmatism accompanied by crustal thickening and assimilation.

1. Introduction

Granitoids are key components of continental crust and provide insights into their magmatic processes and tectonic evolution. In the Kohistan Arc (KA), they form a major part of the upper crust, generated mostly through fractional crystallization of mantle-derived melts (Jagoutz et al., 2009). These granitic plutonic rocks reflect a magmatic history spanning ~ 120 Ma from the Late Jurassic (~154 Ma) to the Tertiary (~30 Ma) (Bouilhol et al., 2013; Jagoutz et al., 2018; Petterson & Windley, 1985). Early granitic magmatism (pre-50 Ma) was predominantly calc-alkaline and arc-related, whereas younger plutons (<50 Ma) show crustal involvement, indicating a transition to arc–continent collision settings (Ahmad et al., 2025a,b; Bouilhol et al., 2013; Jagoutz et al., 2018).

In the central KA, northern Swat Kohistan, the main rock units are metasedimentary and metavolcanic rocks intruded by abundant Late Cretaceous to Early Tertiary plutons (Ahmad et al., 2025a; Jagoutz et al., 2009; Jan & Asif, 1983; Jan & Mian, 1971). Magmatic suites comprise granites, quartz diorites, quartz monzonites, and gabbros, which are linked to arc and collisional tectonic settings (Ahmad et al., 2025b). Previous investigations into the central KA granitoids have primarily emphasized whole-rock geochemistry, zircon U–Pb dating, and Lu–Hf isotope analyses to explore the source characteristics, petrogenesis, and ages of magmatic suites (Ahmad et al., 2025a,b; Jan & Asif, 1983). However, a thorough examination of mineral chemistry to elucidate the pressure and temperature conditions, redox state, and geohygrometry

---

☆ This article is part of a special issue entitled: ‘Evolution of Tethys’ published in Journal of Asian Earth Sciences.

* Corresponding author.

E-mail address: tanveer.ahmad@kit.edu (T. Ahmad).

https://doi.org/10.1016/j.jseaes.2026.107049
Received 14 November 2025; Received in revised form 19 January 2026; Accepted 26 January 2026

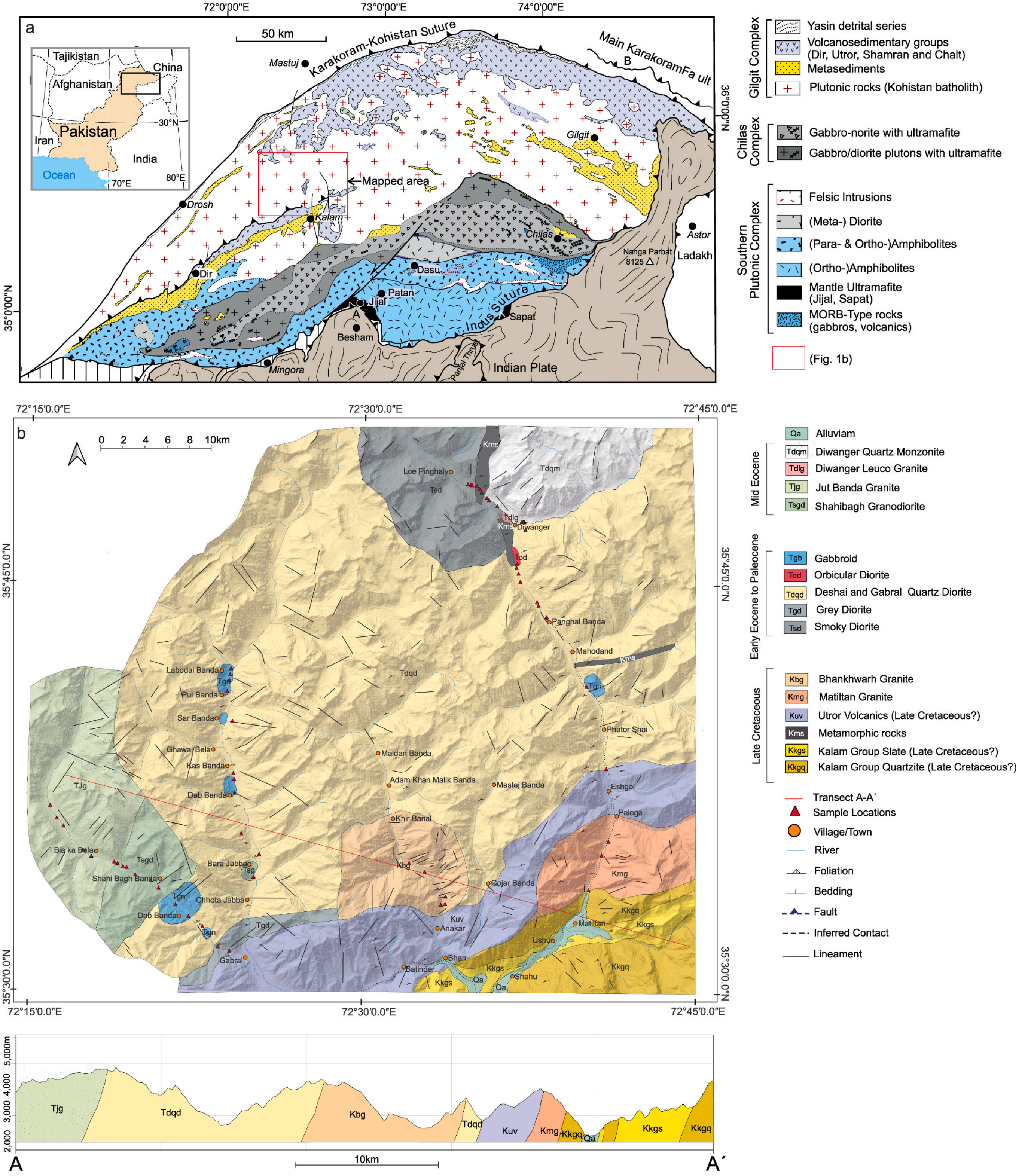

Fig. 1. a) Geological map of the Kohistan island arc showing different lithological units (afterTahirkheli and Jan (1979); Searle et al. (1987), Dhuime et al. (2009), and Jagoutz and Schmidt (2012)). Red box shows the location of the study area. b) Geological map of the central Kohistan magmatic arc in northern Swat, Pakistan, after Ahmad et al. (2025a). (For interpretation of the references to colour in this figure legend, the reader is referred to the web version of this article.)

during the crystallization process has not yet been performed.

The major element compositions of amphibole, biotite, and feldspar offer key proxies for the source characteristics, crystallization conditions, redox states, and water contents of melts (Erdmann et al., 2014; Wones David & Eugster Hans, 1965; Ridolfi, 2021; Ridolfi et al., 2010; Ridolfi & Renzulli, 2012). Accordingly, zircons have been widely used to interpret magma evolution (Barth et al., 2013; Belousova et al., 2002, 2006; Carley et al., 2011; Hoskin, 2005), tectonic setting (Grimes et al., 2007, 2015), oxidation state (Hinton & Upton, 1991; Philpotts, 1970; Trail et al., 2012), and crystallization history (Boehnke et al., 2013;

Ferry & Watson, 2007; Harrison et al., 2008; Watson & Harrison, 1983). Their trace element composition provides information on melting depths and crustal thickness over time (Chapman et al., 2015; Profeta et al., 2015; Tang et al., 2021, 2024).

The granitoids of the central KA provide an opportunity to explore the petrology of the arc crust in different tectonic settings. We provide a comprehensive detailed petrographic description, along with mineral chemistry of amphibole, biotite and feldspar combined with zircon trace elements data derived from numerous Cretaceous to Mid- Tertiary magmatic rocks (quartz diorites, quartz monzonites, granodiorites and granites) from the central KA in northern Swat Kohistan, Pakistan, to reconstruct their parental magma evolution. Additionally, we examine crustal formation processes in central KA, discuss the implications for arc evolution and crustal growth in convergent margin settings, and propose a tentative genetic model.

2. The Kohistan Batholith and northern Swat Kohistan Geology

The Kohistan Batholith, covering a third of the KA, along with its eastern extensions, i.e. the Ladakh and Gangdese batholiths, is part of calc-alkaline magmatic arc exposed across NW Pakistan, India, and China. This arc formed via intra-oceanic subduction of the Neo-Tethys oceanic lithosphere, followed by collision with the Eurasian and Indian plates (Bouilhol et al., 2013; Heuberger et al., 2007; Jagoutz et al., 2018; Jan and Howie., 1981; Khan et al., 1993; Petterson, 2010; Petterson & Windley, 1985; Pudsey et al., 1985; Schaltegger et al., 2002.; Searle et al., 1999). The Kohistan Batholith comprises a suite of calc-alkaline intrusions, including granites, diorites, tonalites, and gabbros, which were emplaced as plutons, stocks, dikes, and sills (Heuberger et al., 2007; Jan & Asif, 1983; Kazmi & Jan 1997; Khalil & Afridi, 1979; Petterson, 2010, 2019; Petterson & Windley, 1991; Treloar et al., 1996). These intrusions crosscut early island arc volcanics (Chalt and Dras Groups) and metasedimentary rocks of the Gilgit Complex (Khan et al., 1993; Khan et al., 1997; Searle et al., 1987).

Results of U–Pb zircon dating indicate onset of magmatism in the Jurassic (c. 154 Ma, Matum Das intrusion), continuing until the Eocene at c. 23 Ma (Ahmad et al., 2025b; Ali et al., 2024; Bouilhol et al., 2013; Jagoutz et al., 2009, 2018; Schaltegger et al., 2002; Ullah et al., 2025). Bulk rock geochemical and isotopic data (Hf in zircon, Nd–Sr whole rock) confirm a juvenile arc setting from c. 154 Ma to 50 Ma, dominated by mantle-derived magmas with minor crustal input (Bouilhol et al., 2013; Burg & Bouilhol, 2019; Jagoutz et al., 2018). After c. 50 Ma, increasing crustal interaction – from either Indian or Karakoram sources – marks a tectonic shift, constraining the India-KA collision to 50.2 ± 1.5 Ma and the final India–Eurasia collision to 40.4 ± 1.3 Ma (Bouilhol et al., 2013; Burg & Bouilhol, 2019).

The Late Cretaceous to Eocene granitoid and gabbroic plutons of the study area in northern Swat Kohistan (Pakistan) are located c. 100 km north of the city Mingora, at elevations of c. 2000 to 4000 m above sea level. Based on chronological data these granitoids are grouped into three major groups, from oldest to youngest: (1) Matiltan and Bhankhwarh granites (77–71 Ma), (2) Smoky diorite and Deshai-Gabral quartz diorites (63–53 Ma), and (3) Diwanger, Shahibagh, and Jut Banda granitoids (47–44 Ma), (Fig. 1b), (Ahmad et al., 2025a,b; Jan & Mian, 1971; Khalil & Afridi, 1979). These granitoids intrude older metasedimentary and volcanic rocks.

The foliated Matiltan and Bhankhwarh granites are bordered by the Utror (meta)volcanics to the north and south. They are mainly comprised of foliated granites containing rare wall-rock xenoliths. The younger unfoliated, dark-colored smoky diorite occurs NW of the Diwanger confluence, in contact with the Deshai quartz diorite and Diwanger quartz monzonite. The Paleocene Gabral and Early Eocene Deshai quartz diorites, which cover much of the central and northern parts of the study area, are composed of foliated locally unfoliated varieties (Ahmad et al., 2025a,b; Khalil & Afridi, 1979). Mid-Eocene potassic to ultra-potassic granites are found in the northeastern (Diwanger) and western (Shahibagh) parts of the study area, intruding the Deshai–Gabral quartz diorite. These younger granitoids are typically non-foliated to weakly foliated and display porphyritic textures. The Gabbroic rocks exhibit a darkish green color and massive texture and form 1–1.5 km wide plugs or dykes within the Gabral and Deshai quartz diorite (Ahmad et al., 2025a). The small orbicular diorite-norite plug near Deshai, described in detail by Symes et al., (1987), probably also belongs to this phase of magmatism.

3. Analytical methods

3.1. Electron microprobe analysis

The mineral compositions of amphibole, biotite, and feldspar from twelve selected samples from seven granitoids were analyzed, comprising the Late Cretaceous Matiltan Granite (MG) and Bhankhwarh Granite (BG), Paleocene Gabral Quartz Diorite (GQD), Early Eocene Deshai quartz diorites (DQD), as well as the Mid Eocene Diwanger quartz monzonite (DQM), Shahibagh granodiorites (SGD), and Jut Banda granites (JBG). The analyses were carried out using a JEOL JXA 8530F electron microprobe-analyzer (EPMA) at Goethe University Frankfurt (Germany), using an acceleration voltage of 15 kV and a beam current of 20nA. Amphibole, biotite, and feldspar were measured using a broadened beam with a diameter of 10 μm. The counting times for all elements, except for Na and K, were 20 s on the peak and 10 s on the background. For Na and K, measurement times of 10 s for the peak and 5 s for the background were applied.

3.2. Zircon preparation, imaging and trace element analyses

Zircon fractions were concentrated by panning 7 granitoid samples, the same investigated by EPMA. Subsequently, up to 100 grains per sample were handpicked under ethanol using a binocular microscope, and mounted on adhesive tape and Au-coated for 10 s. The crystals were investigated for their morphologies by using back-scattered electron (BSE) images produced by a TESCAN VEGA II scanning electron microscope at Institute of Applied Geosciences (IAG) at Karlsruhe Institute of Technology (KIT), Germany. Subsequently, the same grains were cast in epoxy, grinded and polished to expose their interior structure. The latter were made visible by cathodoluminescence (CL) imaging, carried out at the Institute of Functional Interfaces at KIT, using a Quattro S ThermoFisher Scientific Environmental Scanning Electron Microscope (ESEM).

Based on CL images, the most pristine zircon grains/domains, showing no fractures or alteration zones, were measured in situ for trace elements by laser ablation–sector field–inductively coupled plasma–mass spectrometry (LA-SF-ICP-MS) at IAG (KIT, Germany). Analyses were performed using a laser spot diameter of 30 μm, a laser pulse rate of 7 Hz, and an energy density of 5.6 J/cm^2. Following blocks of 30 zircon analyses, the reference glass NIST612 and reference zircon GJ1 were analyzed. Reference glass NIST612 was used as the external standard, and the silica content of zircon was used as the internal standard (fixed at 32.7 wt% SiO_2). The trace element contents obtained from the reference zircon GJ1 are within uncertainties of the published values (Liu et al., 2010). The results of the trace element analyses of 150 zircon grains and the reference material are listed in the ESM (Table. S1.4).

4. Results

4.1. Petrography

4.1.1. Late Cretaceous Matiltan and Bhankhwarh granites

The Matiltan and Bhankhwarh granites are weakly gneissose, medium-grained, and exhibit hypidiomorphic to allotriomorphic textures ranging from equigranular to subequigranular (Fig. 2a-c). Based on visual estimates and semiquantitative X-ray diffraction (XRD) analysis,

Table 1
Petrographic summary of granitoids from the central Kohistan Arc.

Rock Name	Major phases	Modal %	Accessory phases	Petrographic observation
Matiltan Granite	Pl	25–50%	Mgn	Medium grained (1–5 mm),
	Qz	27–40%	Ilm	weakly gneissose,
	Afs	07–10%	Ap	equigranular,
	Bt	05–06%	Zr	and hypidiomorphic to allotriomorphic.
	Hbl	0–1%		
Bhankhwarh Granite	Qz	44–56%	Mgn	Medium to coarse grained (>5mm),
	Pl	25–40%	Ilm	weakly to distinctly gneissose,
	Afs	7–12%	Ep	subequigranular,
	Bt	6–15%	Ap	and hypidiomorphic to allotriomorphic.
	Hbl	0–1%	Zr	
Gabral Quartz diorite	Pl	45–81%	Mgn	Medium-grained,
	Qz	18–32%	Ilm	distinctly to weakly gneissose,
	Afs	0–2%	Ap	equigranular,
	Hbl	5–16%	Zr	and hypidiomorphic to allotriomorphic.
	Bt	5–11%	Ttn	
Deshai Quartz Diorite	Pl	45–62%	Mgn	Medium-grained,
	Qz	19–24%	Ilm	distinctly to weakly gneissose,
	Afs	0–2%	Ap	equigranular,
	Hbl	5–21%	Zr	and hypidiomorphic to allotriomorphic.
	Bt	2–05%	Ttn	
Shahibagh Granodiorite	Pl	47–48%	Mgn	Medium-grained, massive,
	Qz	23–25%	Ilm	equigranular to sub-equigranular,
	Afs	05–10%	Ap	sub-porphyritic,
	Hbl	08–10%	Zr	and idiomorphic to hypidiomorphic.
	Bt	05–10%	Ttn	
Diwanger Quartz Monzonite	Afs	30–42%	Mgn	Medium to-coarse grained,
	Pl	20–30%	Ilm	inequigranular, massive,
	Qz	14–22%	Ap	mega-porphyritic,
	Hbl	06–14%	Zr	and allotriomorphic to hypidiomorphic.
	Bt	05–08%	Ttn, Aln	
Jut Banda Granite	Afs	23–42%	Mgn	Medium to-coarse grained,
	Pl	24–39%	Ilm	inequigranular, massive,
	Qz	21–40%	Ap	mega-porphyritic,
	Hbl	0	Zr	and allotriomorphic to hypidiomorphic.
	Bt	2–5%	Ttn, Aln	

Pl=Plagioclase, Afs: Alkali Feldspar, Qz: Quartz, Hbl: Hornblende, Bt: Biotite, Mgn: Magnetite, Ilm: Ilmenite, Ap: Apatite, Zr: Zircon; Ttn: Titanite, Aln: Allanite.

all samples were classified as granites. Compared to other granitoids in the area, these granites are notably rich in quartz and contain relatively fewer mafic minerals (Table. 1). Notably, the Bhankhwarh granite is generally more gneissose than the Matiltan granite, often displaying augen-gneiss textures, where plagioclase up to 3 mm in length and quartz phenocrysts (1.5–2 mm) are rotated and aligned parallel to foliation, while the granulated quartz, K-feldspar, biotite, and plagioclase of the finer-grained matrix surround them. A distinctive feature of both granites is the extensive hydrothermal alteration, with plagioclase undergone saussuritization and sericitization, while biotite passed through widespread chloritization. Due to intense late brittle deformation, quartz, plagioclase, and biotite in many of the samples are heavily brecciated.

Plagioclase is medium- to coarse-grained (1–5 mm), euhedral to subhedral, and generally cloudy owing to intense sericitization, which commonly obscures twinning (Fig. 2a). Some altered plagioclase grains display thin, weakly altered margins. These rims contain fine inclusions of sericite and epidote and likely formed through late-stage metasomatism. Perthitic orthoclase with simple twinning and exsolved albite blebs occur infrequently in a few samples. Quartz is fine- to medium-grained (0.3–3 mm), highly fractured, and anhedral with characteristic serrated boundaries. It is also found as small inclusions in potash feldspar, plagioclase, and other quartz crystals. In Bhankhwarh granite, quartz frequently occurs as small, shattered grains resulting from the brittle deformation of larger grains, although some larger but heavily strained quartz relics are also preserved.

Biotite is the abundant mafic mineral in both granites, typically subhedral, and flaky (Fig. 2b, c). In the Bhankhwarh granite, biotite is often preferentially oriented, contributing to the foliation of the rock. Nearly all biotite crystals show varying degrees of chloritization, particularly in the Matiltan granite, and often contain inclusions of ore minerals, apatite, and zircons. Hornblende is present only in the Matiltan granite and is less abundant than biotite. It occurs as subhedral to anhedral grains, often twinned, and contains inclusions of quartz and ore minerals (Fig. 2b, g). Alterations to chlorite were observed locally along the margins of the grains and cracks. Fine-grained secondary minerals such as sericite, epidote, and chlorite are common alteration products of plagioclase, biotite, and hornblende.

4.1.2. *Paleocene to Early Eocene quartz diorites*

The Paleocene to Early Eocene quartz diorites comprise the Deshai and Gabral quartz diorites. The Deshai and Gabral quartz diorites are medium-grained, hypidiomorphic to allotriomorphic, and distinctly or weakly gneissose. Modal compositions, determined by thin section analysis and semi-quantitative XRD, classify all samples as quartz diorite (Table. 1).

Plagioclase is generally coarse-grained, averaging 2 mm in length, although it is also fine-grained in the matrix (Fig. 2d-i). It is mostly euhedral and tabular and commonly contains inclusions of quartz, biotite, hornblende, opaque minerals, and epidote. Most grains are weakly altered and exhibit lamellar twinning (both albite and pericline law). Some plagioclase grains are altered to epidote and sericite, mainly in the cores. Zoning is frequently observed, indicating fluctuating crystallization conditions during plagioclase growth (Fig. 2d). Quartz is present as anhedral grains occupying the interstitial spaces between plagioclase and hornblende, suggesting that it crystallized later (Fig. 2e). It also occurs as inclusions within plagioclase, hornblende and biotite. Hornblende is the most abundant mafic mineral, forming euhedral to subhedral grains ranging from 0.5 to 5 mm in length. It is strongly pleochroic, from greenish to brownish, and contains abundant inclusions of plagioclase, quartz, opaque minerals, epidote, and titanite, resulting in a poikilitic texture (Fig. 2e-i). Hornblende often shares straight grain boundaries with plagioclase, indicating co-crystallization of the two minerals. Some hornblende grains show marginal alteration to chlorite. Biotite is the second most abundant mafic mineral. It occurs as medium-grained euhedral flakes adjacent to plagioclase and hornblende and commonly contain inclusions of quartz, apatite, zircon, titanite, and opaque minerals (Fig. 2f). Biotite exhibits yellowish-brown to brownish pleochroism. Notably, in some of the samples intense pleochroism is observed, likely due to Fe or Ti enrichment. Marginal or fracture-related alterations in chlorite are common.

Opaque minerals, including magnetite and ilmenite, are randomly distributed in the matrix and occur as inclusions in amphibole and biotite (Fig. 2i). Titanite and opaque phases are mostly interstitial to biotite, suggesting a late magmatic origin. Titanite and apatite are also present as fine inclusions within plagioclase, quartz, and biotite. Zircon appears as well-developed euhedral crystals enclosed by biotite. Chlorite

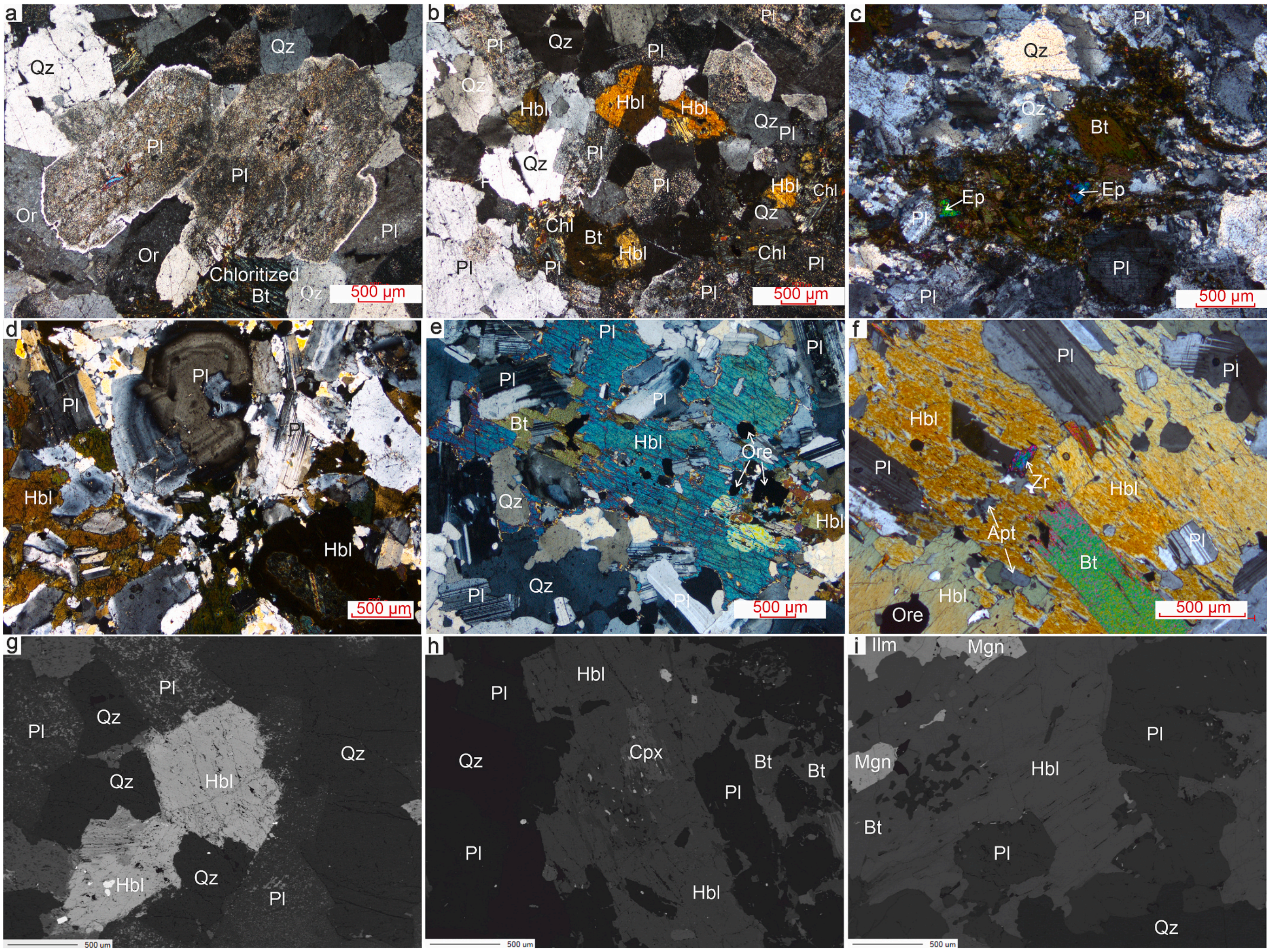

Fig. 2. Microphotographs showing important petrographic features of the Matiltan Granite (a, b, g), Bhankhwarh Granite (c), Gabral Quartz Diorite (d, e, h), and Deshai Quartz Diorite (f, i). (a) Euhedral, intensely altered (sericitized) plagioclase (Pl) grains with weakly altered margins of sodic plagioclase next to orthoclase (Or), anhedral quartz (Qz), and chloritized biotite (Bt); (b) fine-grained hornblende (Hbl) with twinning intergrown with chloritized biotite, plagioclase, and quartz; c) biotite along with interstitial quartz; relics of quartz (some showing straining) and plagioclase are surrounded by recrystallized quartz; epidote (Ep) is associated with biotite; d) euhedral to subhedral plagioclase display polysynthetic twinning and oscillatory zoning, next to hornblende and quartz; e, f) poikilitic hornblende hosting plagioclase, biotite, quartz, zircon (Zr), apatite (Ap) and ore mineral inclusions; g) Back-scattered electron (BSE) image of euhedral hornblende and plagioclase along with subhedral quartz; h) hornblende containing clino-pyroxene relics also including several plagioclase and magnetite (Mgn) grains; i) poikilitic hornblende containing several plagioclase, magnetite and ilmenite (Ilm) grains.

is present as an alteration product of both biotite and hornblende, particularly along the cracks and grain margins. Sericite and epidote commonly replace plagioclase. Epidote is also associated with biotite.

4.1.3. Mid Eocene granitoids (Shahibagh, Diwanger and Jut Banda)

Based on their texture and modal mineralogy, the Mid-Eocene granitoids are further classified into the Shahibagh granodiorite, Diwanger quartz monzonite, and Jut Banda granite (Table. 1; Fig. 3). The Shahibagh granodiorite is massive, medium-grained, equigranular to sub-equigranular, sub-porphyritic, and exhibits idiomorphic or hypidiomorphic textures. Compared to the other mid-Eocene granitoids, the Shahibagh granodiorite contains abundant unaltered plagioclase, a lower amount of K-feldspar, and a notable hornblende content. The Diwanger quartz monzonite and Jut Banda granite are massive and heterogranular, with mega-porphyritic textures, and allotriomorphic to hypidiomorphic. The Diwanger quartz monzonite and Jut Banda granite are distinguished from other granitoids by the presence of coarse-grained phenocrysts of K-feldspar (both orthoclase and microcline) and zoned plagioclase, ranging from 5 mm to 1 cm in length, set within a medium-grained matrix consisting of K-feldspar, plagioclase, quartz, biotite, amphibole, titanite, minor apatite, and zircon. Compared to other granitoids in the study area, these rocks are notably porphyritic and rich in K-feldspar, although minor non-porphyritic, medium-grained varieties with high quartz and low mafic mineral content are locally associated with these plutons. Unlike the Shahibagh granodiorite and Diwanger quartz monzonite, the Jut Banda granite lacks hornblende.

K-feldspar occurs as euhedral crystals forming large tabular orthoclase phenocrysts up to 1 cm in length and display micro-perthitic textures in both Diwanger quartz monzonite and Jut Banda Granite, characterized by albite exsolution lamellae (Fig. 3a, b). It commonly shares straight grain boundaries with plagioclase, implying the co-crystallization of feldspars. Orthoclase grains frequently enclose plagioclase and quartz inclusions. Plagioclase occurs as medium-grained crystals in the groundmass and as large phenocrysts up to 5 mm across, although they are consistently less abundant than K-feldspar (Fig. 3c–e). Plagioclase is euhedral to subhedral and tabular in shape and frequently exhibits concentric zoning, with some grains containing over a dozen oscillatory zones (Fig. 3c). Quartz is less abundant than in other granites in the study area. It typically appears as fine- to medium-grained and

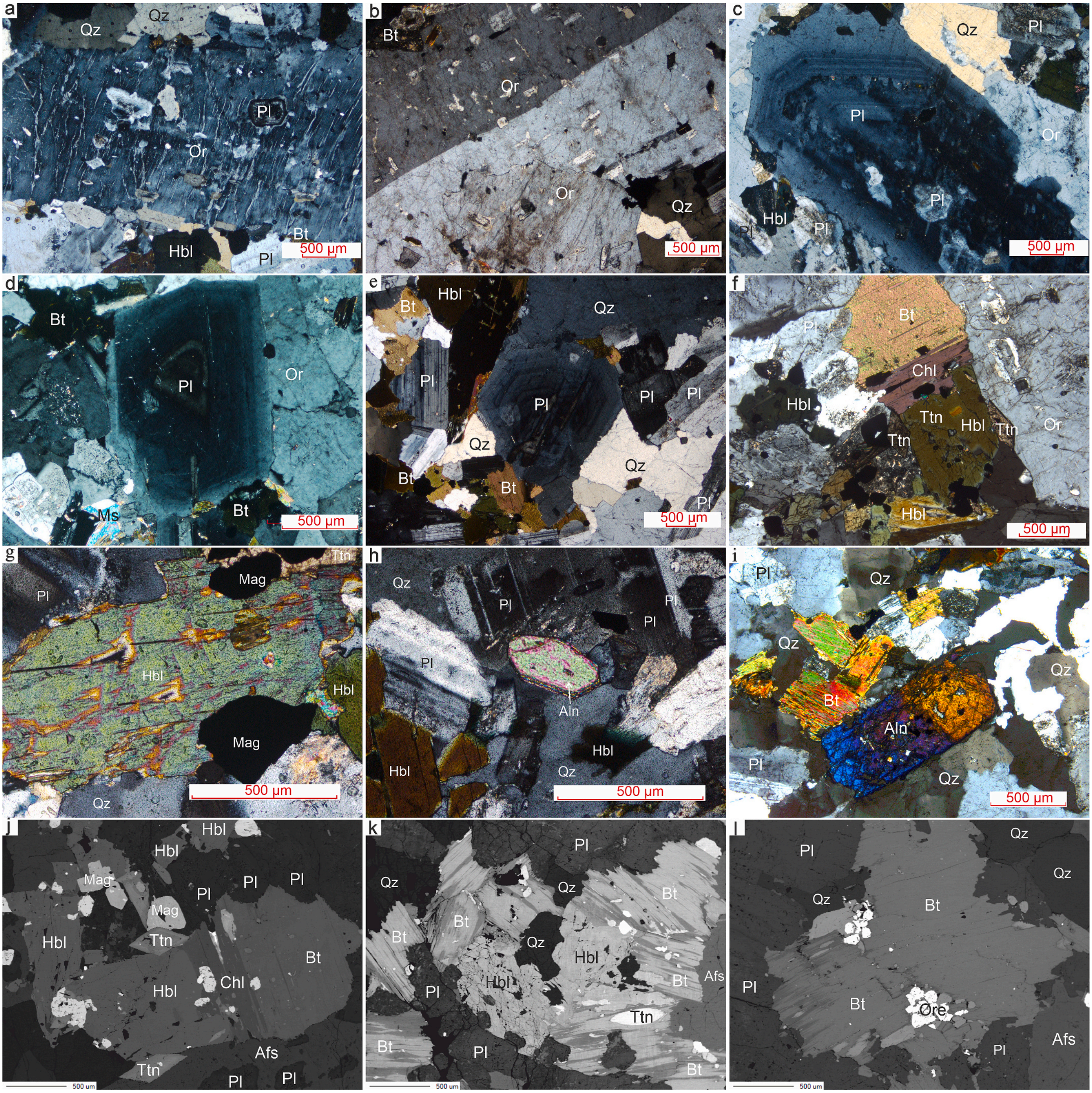

Fig.3. Microphotographs showing important petrographic features of the Diwanger quartz monzonite (a, c, f, j), Shahibagh granodiorite (d, g, h, k), and Jut Banda granite (b, d, I, i): (a) perthitic orthoclase phenocrysts (Or) with spinal-shape and bleb-like albite exsolutions rests in a matrix of zoned plagioclase (Pl), quartz (Qtz) and hornblende (Hbl), Pl occurs as inclusions in Or; (b) orthoclase with Carlsbad twinning hosting quartz, plagioclase, and biotite (Bt) inclusions; (c) oscillatory zoning in plagioclase with inclusions of other plagioclase grains; sericitized plagioclase core surrounded by a weakly altered margin next to quartz and hornblende; (d) plagioclase displaying sector zoning in the top left portion. K-feldspar grains having straight grain boundary contact with plagioclase are also present, along with minor biotite; (e) predominantly euhedral plagioclase grains showing polysynthetic twinning along with biotite and subhedral quartz; oscillatory zoning within plagioclase grain can be seen in the center; (f) biotite grain with magnetite inclusions is chloritized along the margin and associated with hornblende, titanite, and orthoclase; (g) coarse hornblende crystals hosting biotite inclusions and associated zoned plagioclase, quartz, and magnetite grains rimmed by titanite; h) subhedral allanite grain associated with plagioclase, quartz, and brownish and bluish hornblende; i) euhedral, zoned allanite along with chloritized biotite, and anhedral quartz, and plagioclase. Note that quartz grains are mostly undulous, but the irregular, yellow white grain on the right of allanite appears to be poikilitic; j) Back-scattered electron (BSE) image showing biotite grain chloritized along the margin. Euhedral hornblendes associated with titanite, and magnetite are also present; k) BSE image showing hornblende grains surrounded by biotite. Titanite and magnetite occur as inclusions within biotite; l) BSE Image showing euhedral biotite grain containing abundant ore mineral inclusions, surrounded by plagioclase and quartz. (For interpretation of the references to colour in this figure legend, the reader is referred to the web version of this article.)

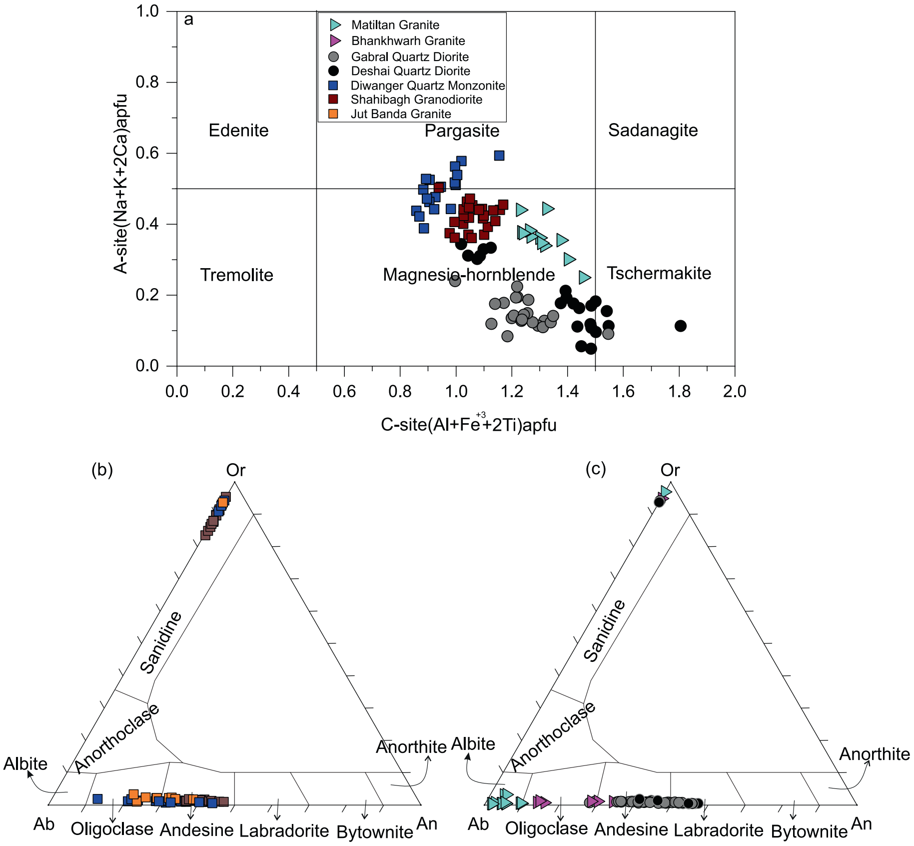

Fig. 4. Chemical composition of amphibole (a) and feldspar (b, c) in granitoids of the Kohistan arc. (a) Composition of amphibole in A-C-site diagram after Hawthorne et al. (2012), a.p.f.u. – atoms per formula unit. (b, c) An-Ab-Or ternary feldspar diagram after Deer et al. (2013).

anhedral in feldspar interstices (Fig. 3e), often with sutured boundaries and shows undulous extinction. Some fine quartz grains with serrated edges fill the spaces between large feldspar phenocrysts, whereas others are enclosed by orthoclase and plagioclase as tiny inclusions.

Hornblende is a common mafic mineral in both the Diwanger quartz monzonite and Shahibagh granodiorite (Fig. 3f, g, j, k). It is medium- to fine-grained, often marginally embayed and poikilitic, and contains inclusions of ore titanite, quartz, magnetite, and zircon. Some hornblende grains exhibit simple twinning and are typically euhedral, subhedral, and prismatic. Alteration to chlorite is observed in several hornblende grains (Fig. 3f, j). Biotite, although less abundant than hornblende, is present as medium-sized, subhedral flakes that exhibit pale yellow to dark brown pleochroism (Fig. 3f, j-l). It is frequently chloritized along grain margins and cleavage planes and hosts inclusions of quartz, ore minerals, titanite, apatite, and zircon.

Titanite occurs as euhedral prismatic crystals and as inclusions within biotite and hornblende (Fig. 3f) and contains inclusions of magnetite, ilmenite, apatite, and zircon. Zircon and allanite are common accessories forming euhedral inclusions within biotite, hornblende, quartz, feldspar, and titanite (Fig. 3f-i). The occurrence of titanite as an inclusion in hornblende suggests their synchronous crystallization, with titanite being incorporated during hornblende growth. The inclusion of zircon, magnetite, and ilmenite within titanite implies that these minerals predate titanite and amphibole. Sericite and chlorite are common alteration products of plagioclase and biotite.

4.2. *Mineral chemistry*

The chemical compositions of amphibole, biotite, and feldspar were determined by EPMA (ESM Table. S1.1-1.3). To illustrate the petrographic variation across all plutons, two representative samples were selected from each of the following plutons: Matiltan Granite, Bhankhwarh Granite, Gabral Quartz Diorite, Deshai Quartz Diorite, Diwanger Quartz Monzonite, Shahibagh Granodiorite, and Jut Banda Granite.

4.2.1. *Amphibole*

The structural formula of amphibole was recalculated based on anhydrous 23 oxygen, with the total number of cations adjusted to 13 ESM (Table. S1.1). The Fe^{3+}/Fe^{2+} ratio was subsequently estimated using charge balance calculations. Most of the studied amphiboles exhibit A-site occupancy of < 0.5, except for the Diwanger quartz monzonite, where half of the analyses have A-site occupancy of > 0.5. In all samples the molar ($C = Al + Fe^{3+} + 2Ti$) apfu occupancy values exceed 0.5.

According to the IMA classification scheme of Hawthorne et al. (2012), most of the amphiboles from all plutons are classified as magnesio-hornblende, with variable A and C site occupancy (Fig. 4a). Only a few analyses from the Deshai and Gabral quartz diorites also plot in the tschermakite field, and half of the analyses from the Diwanger quartz monzonite in the pargasite field. The primary green magmatic amphiboles in all samples are always magnesio-hornblende or pargasite, whereas the secondary brown amphiboles in the Gabral and Deshai quartz diorites are tschermakites.

4.2.2. *Feldspar*

Plagioclase is the predominant feldspar in the studied granitoids. Individual grains within all units generally display variations in anorthite content, reflecting the observed compositional zoning. Plagioclase cores commonly show higher anorthite content, although the zoning patterns can also be complex in all samples. Results of EPMA indicate the following compositional variations for plagioclase presented as anorthite content ($An{=}Ca/Ca + Na + K$, in mol%): Matiltan granite: Albite ($An = 2$–10), Bhankhwarh granite: mostly Oligoclase ($An = 14$–34),

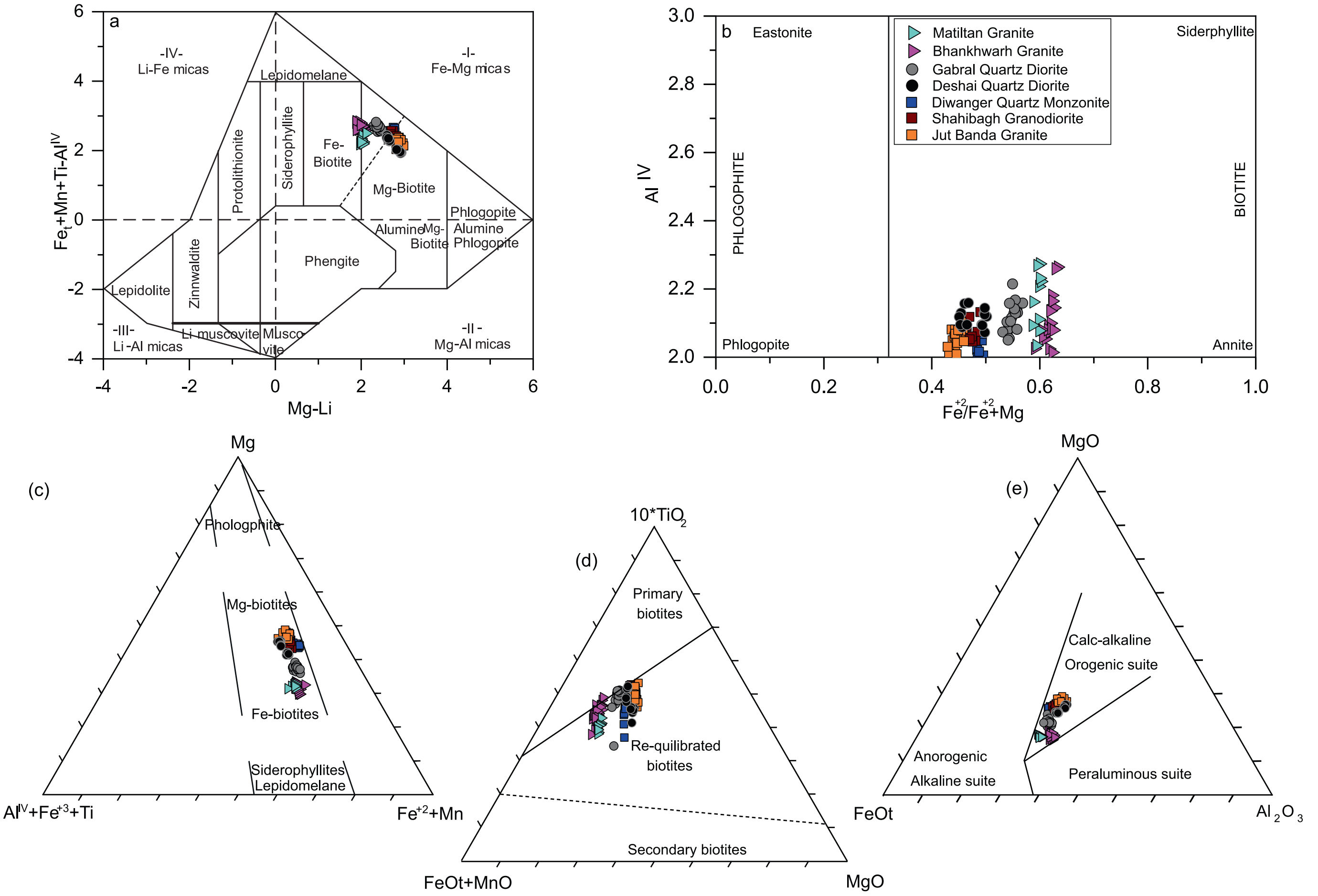

Fig.5. a) Biotite of late Cretaceous to mid-Eocene granitoids of the Kohistan arc presented in (a) classification diagram of biotite afterTischendorf et al. (1997); b) chemical composition and classification diagram after (Deer et al., 2013); (c) (Al^{IV} + Fe^{3+}+Ti)–Mg–(Fe^{2+}+Mn^{2+}) ternary diagram after Foster (1960) showing composition of biotite (d) 10*TiO_2-FeOt + MnO-MgO ternary plot after (Nachit et al., 2005); (e) Tectonic classification of the same biotite after Abdel-Rahman (1994). Element contents in all diagrams are molar contents, calculated from formula units calculated H_2O-free on 22 oxygens.

Gabral & Deshai quartz diorites: Andesine to Labradorite (An = 28–55), Shahibagh granodiorite: Andesine (An: 36–47), Diwanger & Jut Banda plutons: Oligoclase to Andesine (An = 12–43). For details see Fig. 4b, c, and ESM (Table. S1.2). The composition of potassium feldspars varies only slightly from orthoclase to perthite (from $Or_{98.9}Ab_{1.0}$-$An_{0.1}$ to $Or_{83.4}Ab_{0.5}An_{16.1}$; Fig. 4b, c).

4.2.3. Biotite

Microprobe analysis was carried out on biotite from late Cretaceous to Tertiary granitoids. The structural formula was calculated H_2O-free based on 22 oxygen (Table. S1.3). Representative analyses are shown in Fig. 5Aa-e and listed in ESM (Table. S1.3). Biotite in individual granites show little compositional variations, and only small differences among the different plutons (Fig. 5). All biotite analyses yield a molar Fe^{2+}/(Fe^{2+} + Mg) ranging from 0.42 to 0.62, and Al^{iv} = 2.0–2.3 a.p.f.u. (atoms per formula unit), placing them in the annite–siderophyllite field in the classification diagram of Deer et al. (2013), and in the fields for Mg-Biotite in the binary and ternary diagrams of (Tischendorf et al., 1997), and (Foster, 1960), except some analysis from the biotite from the Matiltan and Bhankhwarh granites, which plot in the field for Fe-Biotite (Fig. 5a-c). In the ternary diagrams of Nachit et al. (2005) and Abdel. R (1994), biotite of all granites plot in the field of re-equilibrated (magmatic) biotite, and of calc-alkaline orogenic suites, respectively (Fig. 5d, e).

4.3. Zircon morphology and internal structures

In the investigated samples, most of the recovered zircon grains are non-fragmented and show perfect euhedral shapes. Zircon populations from the Late Cretaceous Matiltan and Bhankhwarh granites (MN43 and BK1) exhibit well-developed {101} pyramidal faces along with {100} prisms (Fig. 6a, b). In contrast, zircons from the Gabral Quartz diorite (GN5) and Deshai diorite (MN1) display more diverse morphologies, characterized by {100} prisms with moderate proportions of {110} prisms along with {101} and {211} pyramids of variable size (Fig. 6b). Zircon grains from the Mid Eocene Diwanger quartz monzonite (D1), Shahibagh granodiorite (GN15), and Jut Banda granite (GN41) consistently exhibit prominent {101} and {211} pyramids along with {100} and {110} prism (Fig. 6b).

Based on Pupin's typological classification (Pupin, 2024, 1980), zircon morphologies of the Cretaceous Matiltan and Bhankhwarh granites (MN41, BK1) indicate a zircon crystallization temperature in the range of 750 and 850 °C. In comparison, zircons from the Gabral quartz diorite yield slightly higher temperature ranging from 800 to 850 °C and even higher for Early Eocene Deshai quartz diorites (800 to 900 °C). The Mid Eocene Diwanger, Shahibagh, and Jut Banda granitoids again yield relatively low temperatures between 750 and 850 °C (Table 2).

Zircon grains from all granitoid samples are euhedral, transparent, and generally ≤ 100 μm in length. In the Cretaceous Matiltan (MN43) and Bhankhwarh (BK1) granites, zircons display prominent oscillatory

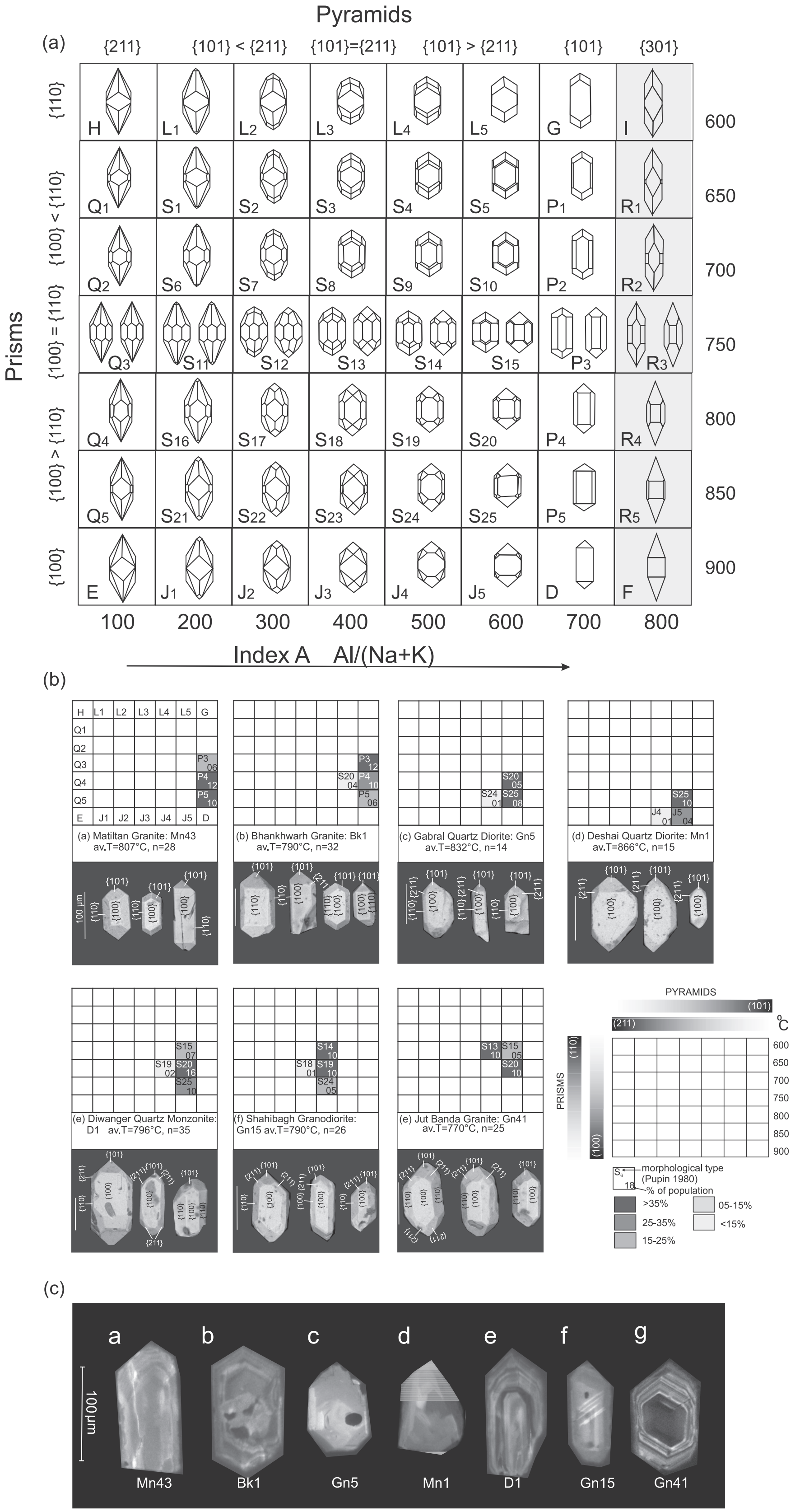

Fig. 6. (a) Zircon typology scheme of Pupin (1980); b) distribution of zircon typologies, and c) representative internal structures of zircon revealed by cathodoluminescence (CL) images of different granitoids.

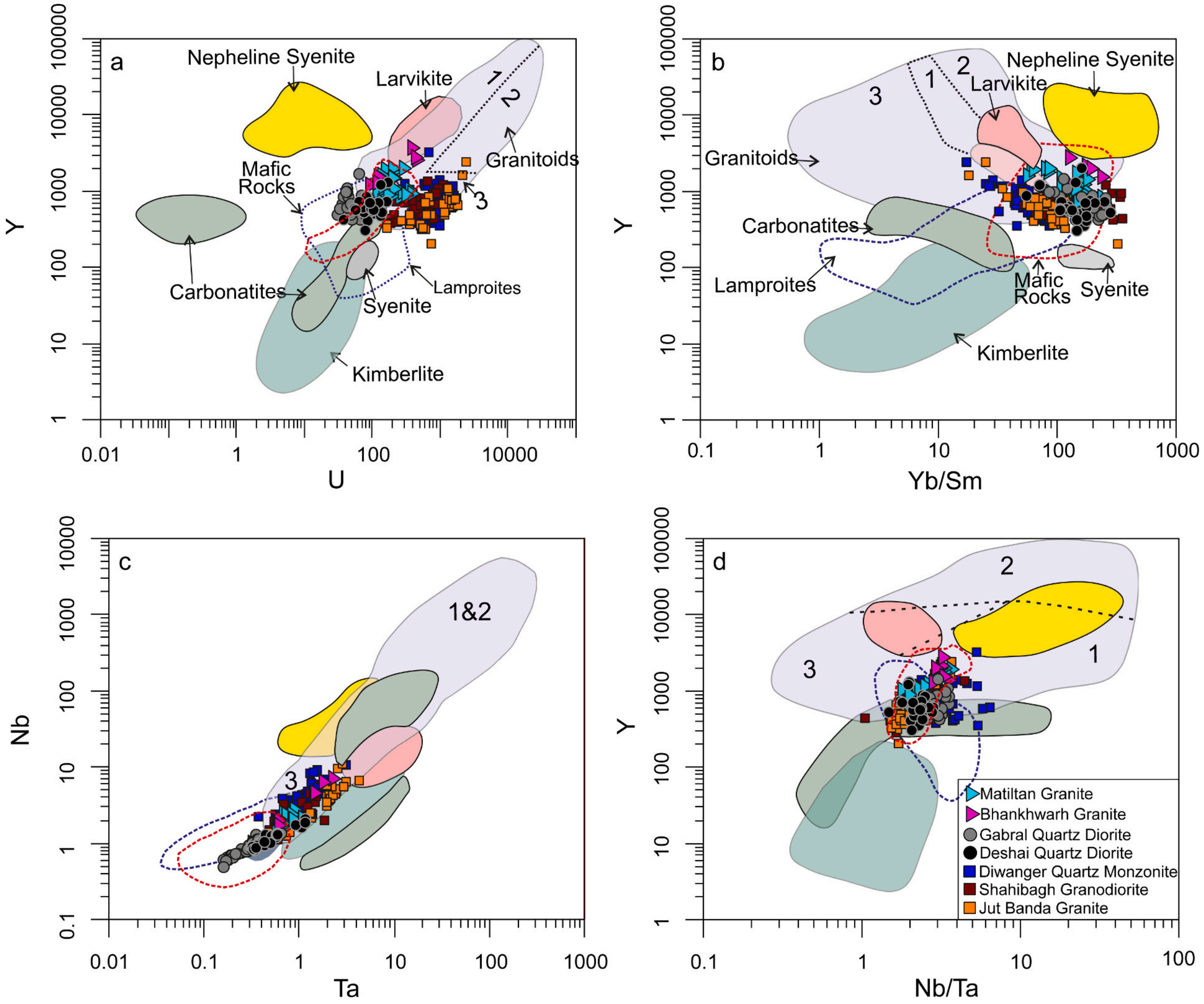

Fig. 7. (a–d) Plots of zircon trace element composition. Compositional fields of parent magma composition after Belousova et al. (2002). 1. Aplite and leucogranites; 2. granites; 3. granodiorites and tonalites.

zoning, particularly on the rims, whereas cores exhibit weaker or absent zoning (Fig. 6c). Zircons from the Paleocene Gabral (GN5) and Early Eocene Deshai (MN1) quartz diorites are euhedral and morphologically uniform, exhibiting weak or no oscillatory zoning (Fig. 6c). In contrast, zircons from the Mid Eocene Diwanger Quartz Monzonite (D1), Shahibagh Granodiorite (GN5), and Jut Banda Granite (GN42) are relatively larger (100–150 μm), display well-developed crystallographic faces, and exhibit strong oscillatory zoning patterns (Fig. 6c). These later zircons also commonly contained abundant inclusions of apatite and unidentified Fe-Ti oxide minerals.

4.4. *Zircon trace element composition*

A total of 120 zircon grains were analyzed from representative samples of all granitoid plutons, including the Matiltan Granite (MN41:10 zircons), Bhankhwarh granite (BK1:5 zircons), Gabral quartz diorite (GN5:15 zirons), Deshai quartz diorite (MN1:20 zirons), Diwanger quartz monzonite (D1:30 zircons), Shahibagh granodiorite (GN15:20 zirons), and Jut Banda granite (GN19:20 zircons). Major (Zr and Hf) and trace element (including REE) contents were determined in situ for each spot. Si was used as internal standard. The results are listed in ESM Table S1.4.

The Hf concentrations in zircon vary across the samples studied. The Late Cretaceous Matiltan (MN41) and Bhankhwarh (BK1) granites yielded average Hf contents of 5711 ppm and 5813 ppm, respectively. In comparison, the Paleocene to Early Eocene Gabral (GN5) and Deshai (MN1) quartz diorites exhibit higher average Hf concentrations of 6779 ppm and 7297 ppm, respectively. The Mid-Eocene Diwanger Quartz Monzonite (D1), Shahibagh Granodiorite (GN15), and Jut Banda Granite (GN42) display moderate average Hf values of 6896 ppm, 6338 ppm, and 6653 ppm, respectively (Table S1.4).

Among the analyzed trace elements, calcium concentrations were consistently low across all samples, generally occurring in trace amounts (Table. S1.4). Phosphorous concentrations were relatively elevated in the Bhankhwarh granite (BK1), averaging 1428 ppm, whereas values in other samples were typically below 500 ppm, consistent with the expected range for natural zircons reported in previous studies (Ballard et al., 2002; Hoskin et al., 2000; Pettke et al., 2005). When plotted on binary trace element diagrams following Belousova et al. (2002), all zircon samples plot within the granitoid field, except for a few analyses from the Gabral and Deshai quartz diorites, which are situated within the mafic zircon domain (Fig. 7a–d).

In chondrite-normalized trace element diagrams (Fig. 8a–d), all analyzed zircons exhibit pronounced negative anomalies in La and P and in the high-field strength elements (HFSE) such as Nb, and Ti, which substitute for Zr in the zircon structure (Hoskin and Schaltegger., 2003; Van Lichtervelde et al., 2011). A consistent enrichment of Ta over Nb and Ti was observed in all samples (Fig. 8a–d). The concentrations of Ti (≤ 75 ppm), Nb (≤ 62 ppm), and Ta (< 3 ppm) fall within the compositional range of unaltered magmatic zircon (Hoskin and Schaltegger.,

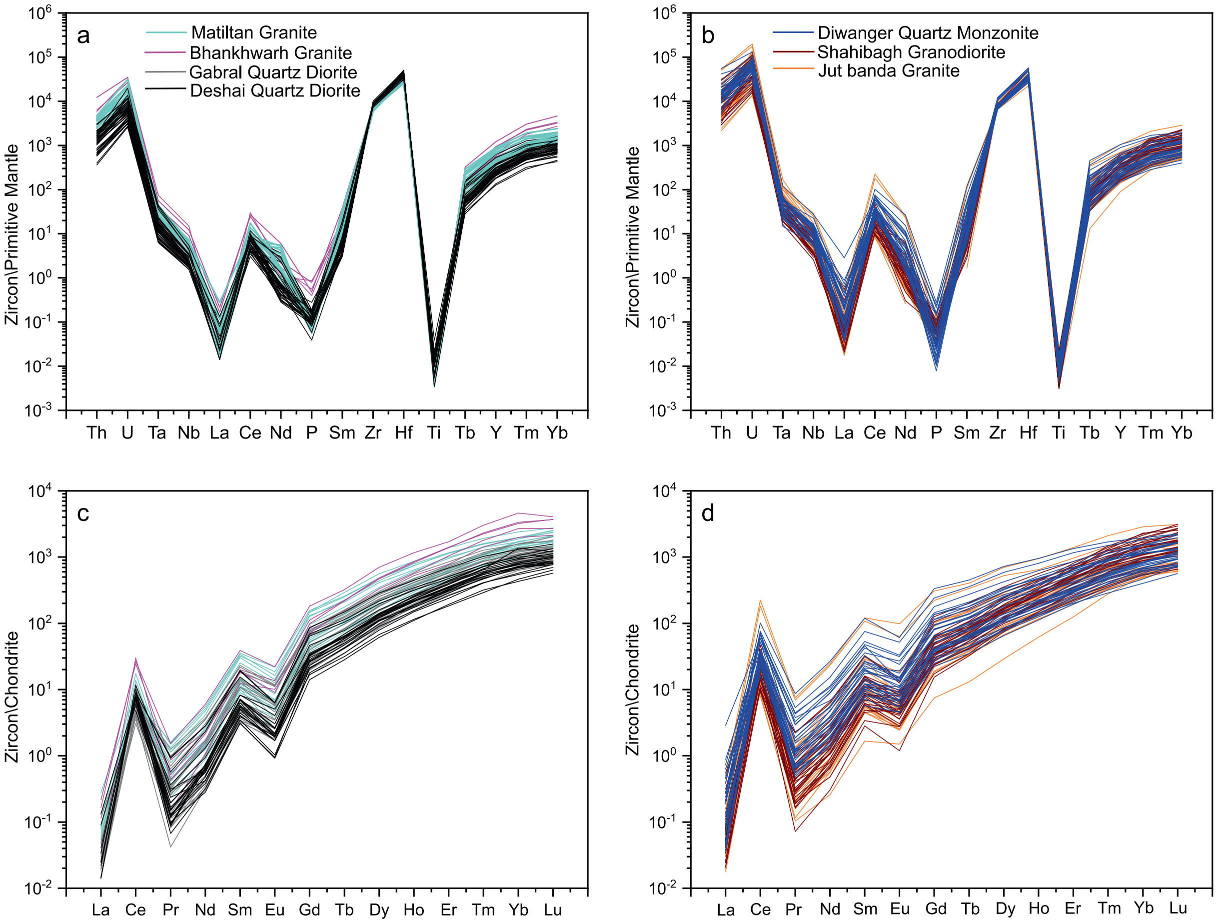

Fig. 8. (a, b) Chondrite-normalized multi-element diagrams for zircons from selected samples of the studied granitoids; (c, d) Chondrite-normalized REE patterns for zircon from selected samples of the studied granitoids. The normalization/reference values for chondrite were obtained from Sun and McDonough (1989*)*.

2003) ().

The total rare earth element (REE) concentrations are rather variable, ranging from 228 to 2318 ppm (ESM Table. S1.4). Chondrite-normalized REE patterns for all samples are characterized by steep slopes, indicating strong enrichment in heavy REEs (HREEs) relative to light (LREEs) and middle rare earth elements (MREEs), and are marked by prominent positive Ce and negative Eu anomalies; typical signatures of unaltered magmatic zircon (Fig. 8c–d) (Belousova et al., 2002; Hinton and Upton, 1991; Hoskin, 2005; Hoskin and Ireland, 2000). The steepness of the REE profiles is expressed as a high average $(Yb/La)_N$ ratio (ESM Table. S 1.4). HREE patterns are nearly identical among all samples, with relatively narrow ranges of elevated $(Yb/Gd)_N$ ratios. In contrast, the LREE segments display greater variability, as reflected by the wide range in $(Sm/La)_N$ ratios (ESM Table. S1.4). MREEs occasionally show slight enrichment, while HREE concentrations consistently fall within the typical range of 10^2–10^4 times chondritic values (Fig. 8c–d). Yttrium concentrations in the analyzed zircons align with values reported for zircons from other granitoids world-wide (e.g., (Barth & Wooden, 2010; Belousova et al., 2006; Hoskin & Ireland, 2000; Orejana et al., 2012.

5. Discussion

5.1. Origin of zircon

The zircons from all the studied granitoids exhibit enrichment in HREE over LREE, as is evident from the steep, positively sloped chondrite-normalized REE patterns. These patterns, coupled with prominent positive Ce, and negative Eu anomalies, are hallmarks of unaltered magmatic zircon (Fu et al., 2009; Zhong et al., 2018), whereas zircon affected by hydrothermal alteration typically displays flatter LREE patterns, due to LREE enrichment that disrupts the original magmatic signature (Cavosie et al., 2006; Geisler et al., 2003; Hoskin, 2005; Pettke et al., 2005). On the La_N vs. Hf diagram, zircons from all samples predominantly plot within the field of magmatic zircons (Fig. 9a), supporting this conclusion. In the Ce_N vs. Hf diagram (Fig. 9b) also, most zircons fall within the igneous field; however, zircons from the Gabral (GN5) and Deshai (MN1) quartz diorites display slightly elevated Ce values, exceeding the normal upper limit of ca. 100 for Ce_N. Some grains from the Diwanger quartz monzonite (sample D1) plot below the lower Ce_N limit for igneous zircon, although the majority still lie within the magmatic field (Fig. 9b). Further validation of the magmatic origin of the analyzed zircons is provided by the Ce/Ce* vs. $(Sm/La)_N$ and the $(Sm/La)_N$ vs. La discrimination diagrams (Fig. 9c, 9d) after Hoskin (2005). Nearly all zircon analyses plot within or near the magmatic fields, with no samples falling into the fields of hydrothermal zircons. The absence of a significant hydrothermal overprint is further supported by Ca vs. U plots after Bouvier et al. (2012) and La_N vs. Pr_N diagrams after El-Bialy & Ali (2013), where all data points fall within the field of unaltered zircon (Fig. 9e, f). These findings are consistent with cathodoluminescence (CL) images, which show sharp oscillatory zoning and a lack of disturbance in the internal textures of zircon (Fig. 6b), further confirming the magmatic origin of all analyzed zircon populations. Taken together, the geochemical data, zircon trace element systematics, and internal structures strongly indicate that all studied zircons crystallized under magmatic conditions without significant overprinting by hydrothermal fluids.

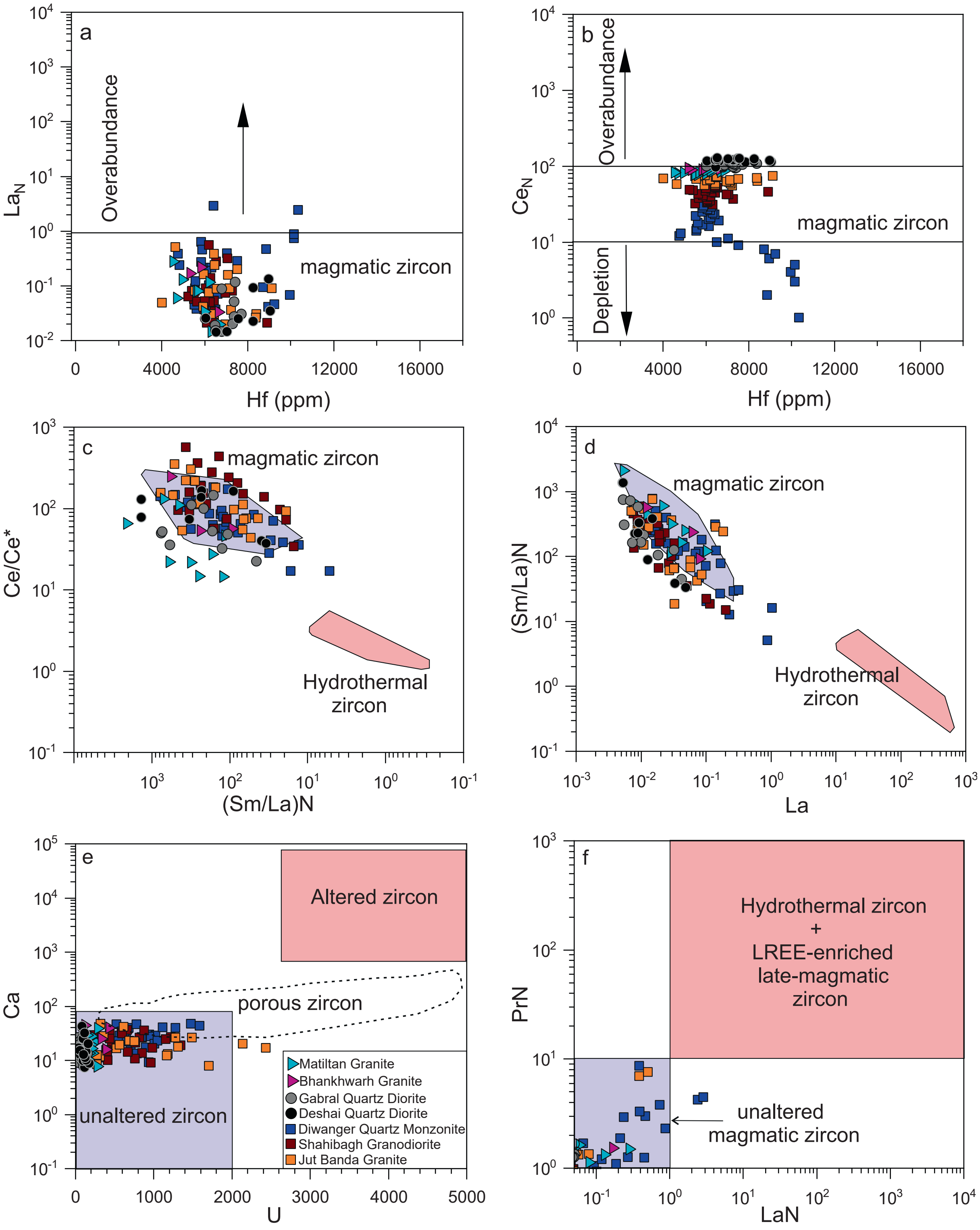

Fig. 9. Diagrams using the trace element compositions of zircon from central KA granitoids (a) Hf vs La_N (Hoskin and Schaltegger, 2003); b) Hf vs. Ce_N (Hoskin and Schaltegger 2003); c) Ce/Ce* vs. (Sm/La)N (Hoskin, 2005); (d) (Sm/La)N vs. La (Hoskin, 2005); e) Ca vs. U (Bouvier et al., 2012), and (f) (La)N vs. (Pr)N (El Bialy, 2013).

5.2. Estimation of physicochemical emplacement conditions of the granitoid magmas

The temperature, pressure, oxygen fugacity, and water content of each pluton were estimated using the mineral chemistry data of plagioclase, amphibole, zircon, and biotite. These physicochemical parameters provide key constraints on the processes governing magma generation and evolution and are essential for reconstructing the thermal and emplacement history of the Late Cretaceous to Early Tertiary plutonic rocks exposed in northern Swat and central KA. The average values derived for each pluton are summarized in Table. 2, while the complete dataset is provided in Supplementary Material (ESM Table. S

Table 2

Summary of pressure, temperature, oxygen fugacity, and H_2O content estimated from various geothermobarometric, oxybarometric and hygrometric calibration for plutonic rocks of the central Kohistan Arc.

Rock type	Age		Amp P (kbar) [a]	Amp P (kbar) [b]	Amp P (kbar) [c]	Amp P (kbar) [d]	Depth (Km) [e]	Pl T(°C) [f]	Amp T (°C) [g]	Amp T (°C) [h]	Bt T (°C) [i]	Ti in ZrnT (°C) [j]	Zr-T (°C) [k]	Hbl logfO_2^l	H_2O melt (%) [m]
Matiltan Granite	Late Cretaceous	Min	3.3	3.1	2.7	2.0	11.7	1010.5	726.0	766.1	602.9	666.1	750.0	−17	3.7
Matiltan Granite	Late Cretaceous	Max	4.4	4.2	3.4	3.3	16.0	1093.3	763.1	794.8	618.1	803.6	850.0	−15	5.5
Matiltan Granite	Late Cretaceous	**Avg**	3.8	3.6	3.0	2.6	13.7	1045.3	745.8	783.0	611.0	721.7	807.1	−16	4.6
Bhankhwarh Granite	Late Cretaceous	Min	…	…	…	…	…	985.8	…	…	601.2	708.4	750.0	…	…
Bhankhwarh Granite	Late Cretaceous	Max	…	…	…	…	…	1011.4	…	…	642.9	736.3	850.0	…	…
Bhankhwarh Granite	Late Cretaceous	**Avg**	…	…	…	…	…	998.5	…	…	618.3	722.2	790.6	…	…
Gabral Quartz- Diorite	Paleocene	Min	2.9	2.8	2.4	1.7	10.4	1088.4	721.7	757.0	634.5	732.0	800.0	−16	4.9
Gabral Quartz-Diorite	Paleocene	Max	3.5	3.4	2.8	3.2	12.9	1140.3	758.2	790.6	663.5	833.4	850.0	−15	8.3
Gabral Quartz- Diorite	Paleocene	**Avg**	3.2	3.0	2.6	2.4	11.4	1119.7	740.2	776.5	654.6	777.6	832.0	−16	5.9
Deshai Quartz-Diorite	Early-Eocene	Min	3.8	3.7	3.0	2.4	13.9	1160.2	751.3	754.4	630.9	699.2	850.0	−15	5.7
Deshai Quartz-Diorite	Early-Eocene	Max	5.6	5.4	4.3	4.1	20.3	1299.3	799.3	821.2	681.7	822.4	900.0	−11	8.5
Deshai Quartz Diorite	Early-Eocene	**Avg**	4.6	4.5	3.6	3.4	16.9	1229.9	774.2	793.7	656.6	770.1	866.6	−14	7.2
Diwanger Quartz-Monzonite	Mid-Eocene	Min	2.7	2.7	2.3	2.7	10.0	1040.4	750.3	767.8	612.1	678.9	750.0	−14	5.2
Diwanger Quartz-Monzonite	Mid-Eocene	Max	5.1	4.9	3.9	4.1	18.6	1098.6	817.8	833.9	651.0	780.8	850.0	−11	6.1
Diwanger Quartz-Monzonite	Mid-Eocene	**Avg**	3.8	3.7	3.0	3.4	14.0	1066.6	780.1	787.3	639.9	722.2	796.0	−13	5.7
Jut Banda Granite	Mid-Eocene	Min	…	…	…	…	…	1088.5	…	…	657.3	653.6	750.0	…	…
Jut Banda Granite	Mid-Eocene	Max	…	…	…	…	…	1141.9	…	…	707.2	773.0	850.0	…	…
Jut Banda Granite	Mid-Eocene	**Avg**	…	…	…	…	…	1115.2	…	…	678.1	702.6	790.3	…	…
Shahibagh Granodiorite	Mid-Eocene	Min	3.8	3.7	3.0	3.0	14.1	1024.9	763.2	767.0	656.2	652.1	750.0	−14	5.8
Shahibagh Granodiorite	Mid-Eocene	Max	4.8	4.6	3.7	3.2	17.4	1071.4	801.6	801.2	690.2	761.4	800.0	−12	7.0
Shahibagh Granodiorite	Mid-Eocene	**Avg**	4.2	4.1	3.3	3.1	15.6	1050.6	785.4	786.2	674.8	695.1	770.0	−13	6.3

P= Pressure, T = Temperature, fO_2= Oxygen fugacity; a= Anderson & Smith (1995), b= Schmidt (1992), c= Mutch et al. (2016), d= Holland & Blundy (1994), e= Schmidt (1992), f= Putirka (2005), g=Putirka (2016), h= Ridolfi (2021), i= Henry et al. (2005), j = Watson & Ferry (2007), k= Pupin (1980), l= Ridolfi (2021), m=Ridolfi (2021). Amp: Amphibole, Pl: Plagioclase, Bt: Biotite, Ti: Titanium; Zr: Zircon.

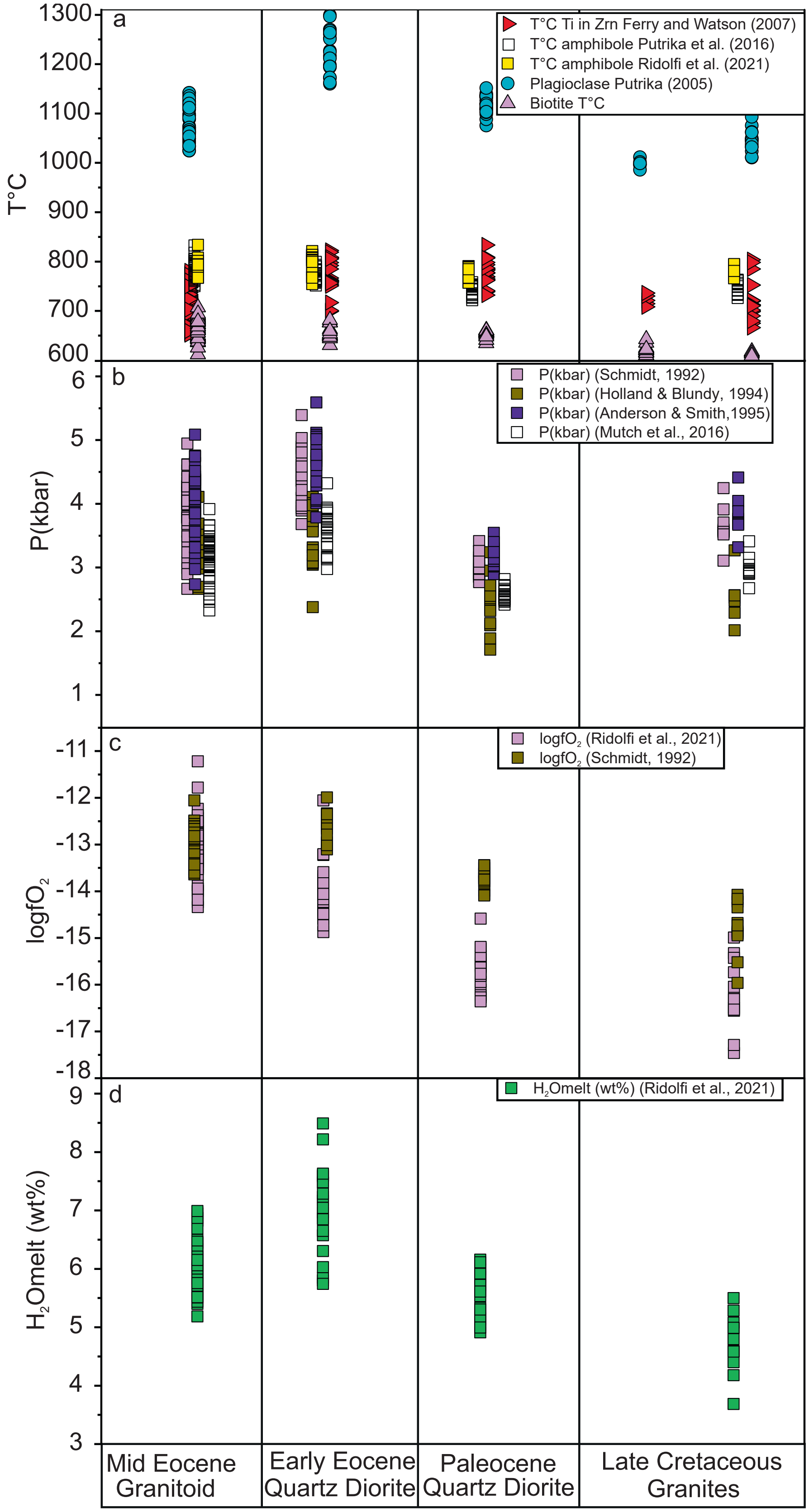

(caption on next page)

Fig. 10. (a) Crystallization temperatures recorded in the central Kohistan Arc granitoids, estimated from mineral thermometry. Symbols represent different minerals, and colors represent different methods (listed in figure). Plagioclase: Crystallization temperatures are calculated using Putirka (2005, equation 23) for plagioclase anorthite content > 10 in equilibrium with whole- rock compositions, Zircon: Crystallization temperatures are calculated using Ferry and Watson (2007) Ti- in-zircon method (equation 15), Amphibole: Crystallization temperatures are calculated using Putirka (2016, equation 5) and Ridolfi (2021), Ti in Biotite temperature after Henry (2005). b) Pressure is calculated using calibrations of Schmidt (1992), Hbl-Pl thermometry after Holland and Blundy (1994), Al in hornblende thermometry after Anderson and smith (1995), and Mutch et al., 2016; c) LogfO_2 are calculated using calibration of Schmidt, 1992 and Ridolfi, 2021; d) H2O in melt are estimated using calibration after Ridolfi, 2021.

1.1 to 1.4).

5.2.1. Temperature of magma emplacement and crystallization

The crystallization sequence inferred from plagioclase, amphibole, zircon, and biotite thermometry across central KA provides crucial insights into the thermal evolution and magmatic history from the Late Cretaceous to the Mid-Eocene. The systematic variation in crystallization temperatures among different minerals and plutons reflects the complex interplay of the tectonic setting, magma source, volatile content, and degree of magma evolution of the Kohistan Arc.

Calculations using plagioclase thermometry after Putirka (2005; eq.2) indicates highest crystallization temperatures (985– 1300 °C) relative to other mineral phases, consistent with the role of plagioclase as an early-crystallizing phase (Fig. 10a; Table 2). The Early Eocene Deshai quartz diorite (1160–1229 °C; An39–57) and Paleocene Gabral quartz diorite (1088–1140 °C; An35-55) records the highest temperatures among the granitoids, indicating their derivation consistent with subduction-related arcs from relatively primitive, mantle-derived magmas emplaced under hotter thermal regimes. In contrast, the late Cretaceous Bhankhwarh granite (985–1011 °C; An10-33) records the lowest plagioclase crystallization temperature, despite its arc affinity, likely reflecting crystallization from relatively more evolved felsic melts. The Mid-Eocene collisional granitoids recorded moderately high plagioclase crystallization temperature (1024–1141; An20-46), reflecting hybrid magma generation during the onset of arc-continental collision when mantle input persisted and was significantly modified by fluids and crustal assimilation.

Amphibole-based crystallization temperature was estimated using the thermometry of Putirka (2016; eq. 5) yielding lower temperature (726–817 °C) than those recorded from plagioclase, reflecting its formation during intermediate magmatic stages. Complementary amphibole temperatures calculated using Ridolfi (2021) calibration yield comparable results (Table. 2). The Early Eocene Deshai quartz diorite yields slightly higher values (751–799 °C) compared to the Paleocene Gabral quartz diorite (721–758 °C) and the Late Cretaceous Matiltan granite (726–763 °C), suggesting hotter arc magmas (Table 2). By the Mid-Eocene, the post-collisional Diwanger quartz monzonite and Shahibagh granodiorite (750–817.8 °C) displayed comparable or even slightly elevated temperatures, indicating that even after collision, the residual mantle heat persisted during arc-continental collision, evolving magma source, and crustal assimilation. These fluctuations in plagioclase and amphibole crystallization temperatures over time may reflect the changing thermal state of the Kohistan arc from cooler, more evolved Cretaceous magmas to hotter primitive mantle-derived melts during the Paleocene and Mid-Eocene. The thermal uplift during the Paleocene and Early Eocene was probably the result of enhanced mantle input and deeper melting, whereas the subsequent thermal stabilization and compositional evolution during the mid-Eocene may correspond to slab break-off or mantle upwelling associated with the transition from intra-arc to continent–arc collision.

Ti-in-zircon across the suite further documents this long-term crystallization trend. The Ti-in-zircon thermometry, using calibration by (Ferry & Watson, 2007), was employed to estimate crystallization temperature which is based on temperature dependent incorporation of Ti in zircon coexisting with rutile. The temperature is calculated using the equation $T°\text{C} = 5080 / (log_{10}(Ti) + 6.01) - 273.15$, (assuming $aSiO_2 = 1$, $aTiO_2 = 0.6$) where Ti is the concentration in ppm measured using LA-ICPMS. The thermometer yields an accuracy of ± 10 °C (Table. 2). The Ti in zircon thermometer yields a broader but generally lower temperature range than that of plagioclase and amphibole, consistent with zircon crystallizing from more evolved and cooler melt fractions (Fig. 10a).

Late Cretaceous zircons from the Matiltan and Bhankhwarh granites yield average Ti-in-zircon temperatures of 723.1 °C and 722.2 °C, respectively, reflecting zircon growth in relatively evolved and cooler magma. In contrast, zircon from the Paleocene Gabral quartz diorite and Early Eocene Deshai quartz diorite extend up to Avg 777.6 °C and Avg 770.1 °C, respectively. These elevated temperatures support zircon crystallization from hotter, less evolved melts, consistent with enhanced mantle input during this magmatic interval. By the Mid-Eocene, zircons from Diwanger quartz monzonite, Shahibagh granodiorite, and Jut Banda granite record relatively low average temperatures of 722.1 °C, 695.0 °C, and 702.6 °C, respectively, suggesting more evolved melts and prolonged cooling histories.

Morphology-based temperature estimates for zircon formation, derived using Pupin's (1980) typological classification, are consistent with Ti-in-zircon results. Estimated crystallization temperatures are 750–850 °C for the Cretaceous Matiltan and Bhankhwarh granites, 800–900 °C for the Paleocene Gabral and Early Eocene Deshai quartz diorites, and 750–850 °C for the Mid-Eocene Diwanger, Shahibagh, and Jut Banda plutons (Table. 2). These similarities confirm the strong temperature control on zircon morphology, particularly the {100}:{110} prism ratio.

Biotite thermometry after Henry (2005) yielded the lowest crystallization temperatures across all plutons, further supporting its role as a late-stage mineral. The calculated temperatures are 601–642 °C for the Matiltan and Bhankhwarh granites, 634–663 °C for the Gabral quartz diorite, 630–681 °C for the Deshai quartz diorite, and 612–707 °C for the younger Mid-Eocene granitoids (Fig 10a; Table 2). These low temperatures mark re-equilibration during magmatic cooling.

Collectively, the crystallization sequence of plagioclase at high temperature, amphibole and zircon formation at moderate temperatures, followed by biotite at lower temperatures, recorded for all plutons, reflects a coherent trend of progressive magmatic crystallization with decreasing temperature. The variations in temperature across different plutons over time can be attributed to a change in the tectonomagmatic regimes: relatively cooler, more evolved granites during the Late Cretaceous intra-arc stage; a significant thermal peak during Paleocene and Early Eocene, linked to more primitive melt and high mantle influx; and a subsequent thermal stabilization during the Mid-Eocene, when tectonic processes is associated with arc–continent collision and magmatism was increasingly influenced by crustal contributions. This integrated record underscores the dynamic interplay among magma differentiation, mantle input, and tectonic setting in governing the thermal evolution of the Kohistan arc.

5.2.2. Emplacement depths of the granitoid plutons

Geobarometric estimation was performed using empirical calibrations of Schmidt (1992), Holland & Blundy (1994), Anderson & Smith (1995), and Mutch et al. (2016). The estimation yields typical uncertainty of < 12%. The amphiboles from the Late Cretaceous to the Mid-Eocene granitoids offer robust constraints on the depth of magma crystallization and emplacement during different tectonomagmatic stages (Fig. 10b). The Late Cretaceous Matiltan granite and Paleocene Gabral quartz diorite record relatively low crystallization pressures, ranging from 3.1 to 4.2 kbar and 2.7–3.4 kbar, respectively,

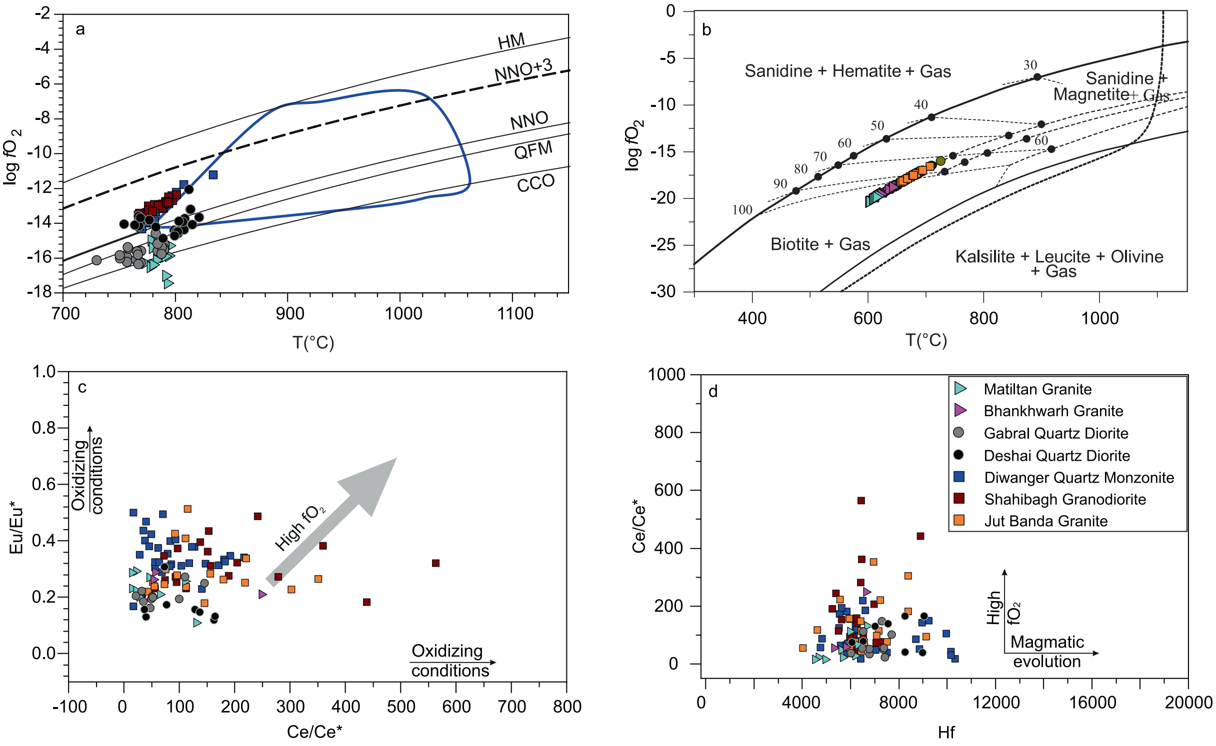

Fig. 11. (a) Log fO_2 versus T diagrams with metal–metal oxide buffers after Hirschmann et al. (2008) for amphiboles in the granitoids of the central Kohistan batholith; b) $\log fO^2$ versus T diagrams of biotite. The dashed line shows the probability in percent of the biotite + gas buffer (Wones, 1989); c, d) Eu/Eu* vs. Ce/Ce* and Ce/Ce* vs. Hf diagrams revealing the oxidation state of the magma from which the studied zircons were crystallized; and e) diagram of T °C versus H_2O concentration of the melt.

corresponding to shallow mid-crustal depth of 11–13 km (Table. 2). In contrast, relatively higher pressures were estimated for the Early Eocene Deshai quartz diorite (3.6–5.8 kbar) and the Mid-Eocene Diwanger and Shahibagh granitoids (2.6–4.9 kbar), indicating a deeper mid-crust emplacement level of 16 to 20 km (Table. 2). This progressive increase in pressure and depth of crystallization over time suggests a progressive deepening of the magmatic differentiation levels, likely associated with the evolving tectonic regime from intra-arc in the Late Cretaceous- Paleocene to the transition period in the Early Eocene to arc-continental collision in the Mid-Eocene.

Amphibole-based pressure estimates are corroborated by the composition of zircon, which provides robust proxies for inferring the depths of magma crystallization. The lack of relationship between Eu/Eu* and trace element ratios such as Th/Yb and U/Yb during the Late Cretaceous to Early Eocene suggests uniform crystallization in a thinner crustal setting, while the positive correlation between Eu/Eu* vs. U/Yb and Th/Yb in the collisional Mid-Eocene granitoids indicates an increase in magma crystallization depths during this time (Fig. 1S). Elevated values of Eu/Eu* suggest higher-pressure crystallization conditions, where the suppression of plagioclase crystallization limits Eu partitioning, thereby diminishing the negative Eu anomaly (Tang et al., 2021, 2024). Concurrent enrichment in U/Yb and Th/Yb ratios likely reflects garnet fractionation at greater depths, as garnet preferentially incorporates Yb over U and Th due to its compatible lattice structure (e.g., (Johnson, 1998).

Collective evidence from amphibole geobarometry and zircon geochemical proxies indicates a temporal shift in the depth of crystallization and source across the studied magmatic suites. The Late Cretaceous to Paleocene granitoids record comparatively low crystallization pressure, suggesting emplacement at a shallow mid-crustal level within a thinner lithospheric crust. In contrast, the transitional Early Eocene and collisional Mid-Eocene granitoids exhibit comparatively high crystallization pressures, indicating emplacement at relatively deep crustal levels within a thicker crust. These findings support a model of progressive magmatic deepening, consistent with the transition of the tectonic regime from arc-related magmatism with shallow-level magma differentiation to arc-continental collisional magmatism marked by deeper magma generation and emplacement.

5.2.3. *Redox condition and water content*

Redox conditions are deciphered from the amphibole chemistry using the calibrations of Schmidt (1992) and Ridolfi (2021). The model estimates oxygen fugacity (fO_2) using amphibole composition through an empirical equation for ΔNNO (relative to the Ni-NiO buffer), which yields an uncertainty of ± 0.3 log units and is valid for Mg-rich calcic amphiboles. Redox conditions show systematic variations across plutonic suites of different ages (Figs. 10c, 11a). The Late Cretaceous Matiltan granite is characterized by relatively low oxygen fugacity (log fO_2 between –17 and –15), indicating lower oxidized conditions during crystallization. Slightly higher fO_2 values (–16 to –15) are calculated for the Paleocene Gabral quartz diorite. The Early Eocene Deshai quartz diorite (–15 to –11) and Mid-Eocene Diwanger and Shahibagh granitoids (–14 to –11) reflect progressively more oxidizing environments, suggesting evolution from low to more oxidized magmatic conditions over time (Table 2). This trend is corroborated by oxygen fugacity estimates derived from biotite composition using the calibration of (Wones David & P. Eugster Hans, 1965) (Fig. 11b). Biotite from the Matiltan and Bhankhwarh granites, as well as from the Gabral quartz diorite, suggests low fO_2 clustering between –20 and –18. In contrast, the Deshai quartz diorite and Mid-Eocene granitoids (Shahibagh, Diwanger, and Jut Banda) record slightly higher fO_2 values (–19 to –16), supporting the amphibole-based redox interpretations.

Zircon geochemistry provides further constraints on magma oxygen fugacity. The Eu/Eu* anomaly in zircon correlates well with the fO_2 values inferred from the amphibole and biotite compositions. Zircons from the Matiltan (Eu/Eu* = 0.11–0.32), Bhankhwarh (0.21–0.34),

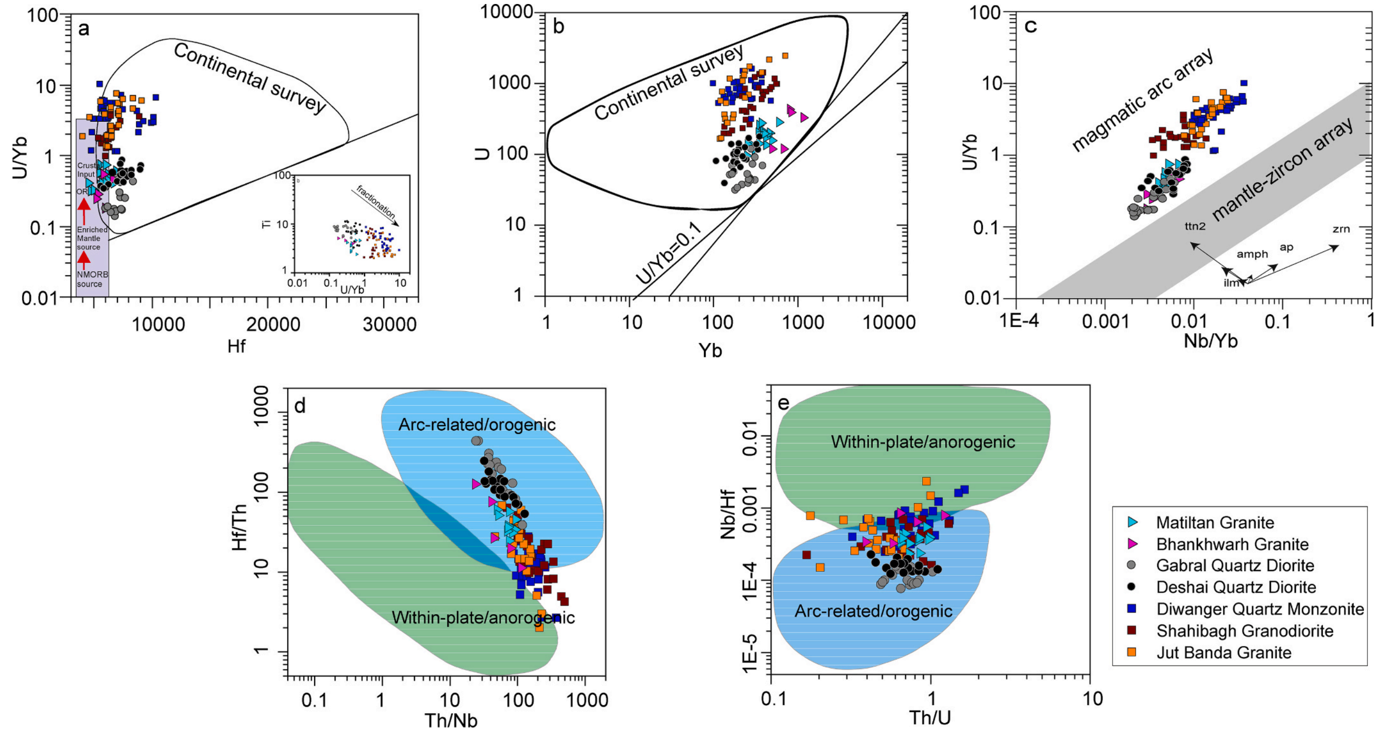

Fig. 12. Tectonic discrimination diagrams using zircon trace elements a) U/Yb vs. Hf and b) U vs. Yb discrimination diagrams after Grimes et al. (2007, 2015); c) U/Yb vs. Nb/Yb tectonic-magmatic source discrimination diagram for igneous zircon after Grimes et al. (2015). Continental series defined by Grimes et al. (2007); d) Th/Nb vs. Hf/Th diagrams after Yang et al. (2012); and e) Th/U vs. Nb/Hf diagram after Hawkesworth and Kemp (2006) for the studied zircons from granitoids of the Central Kohistan Magmatic Arc.

Gabral (0.16–0.27) and Deshai (0.12–0.31) plutons display low Eu anomalies, consistent with their crystallization under reducing conditions, whereas the Mid-Eocene Diwanger, Shahibagh, and Jut Banda granitoids exhibit significantly higher Eu/Eu* values (0.15–0.51), suggesting zircon crystallization under more oxidizing conditions (Table 2). Notably, a positive linear to curvilinear correlation between Ce and Eu anomalies (Fig. 11c) across zircons from all granitoids underscores the control of oxidation state during zircon crystallization cf.(Cao et al., 2011; Hidaka et al., 2002; Orejana et al., 2011; Wang et al., 2013). Since the Eu^{3+}/Eu^{2+} ratio in the melt is a function of oxygen fugacity, and Eu^{2+} is less compatible in zircon than Eu^{3+}, higher oxidation enhances Eu partitioning into zircon, leading to increased Eu/Eu* values (Trail et al., 2012). This supports the conclusion that Mid-Eocene zircons crystallized from more oxidized melts, whereas older plutons formed under low oxidizing conditions. This trend can also be demonstrated by the Ce/Ce* values of zircon (Fig. 11d). Zircons from the Mid-Eocene post-collisional granitoids yield high Ce/Ce* values up to 732, indicative of strongly oxidized magmatic conditions. Under such conditions, Ce^{4+} – which preferentially substitutes for Zr^{4+}, Hf^{4+}, U^{4+}, and Th^{4+} in zircon– is more compatible than the trivalent LREEs such as La^{3+} and Pr^{3+} (Ballard et al., 2002; Hidaka et al., 2002; Trail et al., 2012; Xia et al., 2010). Collectively, the multi-mineral redox proxies reveal a consistent trend toward increasingly oxidized magmatic conditions during magma emplacement from the Late Cretaceous to the Mid-Eocene. This progression likely reflects enhanced crustal assimilation, leading to more oxidized melts associated with postcollisional magmatism.

Water contents of the magma in equilibrium with amphibole is estimated using (Ridolfi, 2021) Amp-TB2 model. This method estimates the H_2O content in the melt with an overall uncertainty of ± 14%. The H_2O content further constrains the magmatic conditions of the studied plutons. The Late Cretaceous Matiltan Granite displays the lowest average H_2O content (~4.6 wt%), suggesting crystallization from a relatively less hydrous magma. In contrast, the Paleocene Gabral Quartz Diorite yields an intermediate water content (~5.9 wt%), indicative of a mixed or variable source. The Early Eocene Deshai Quartz Diorite (~7.2 wt%), and the Mid-Eocene Diwanger Quartz Monzonite, and Shahibagh Granodiorite (~5.7 to ~ 6.3 wt%) suggest more hydrous magmatic conditions, consistent with higher volatile input by slab-derived fluids or crustal assimilation (Fig. 10d).

The integrated temperature, pressure, redox, and volatile data reflect the progressive evolution of the KA from the Late Cretaceous to the Mid-Eocene. The Late Cretaceous Matiltan granite crystallized at mid-crustal depths (3.1–4.2 kbar) under low oxidized conditions (log $fO_2 \approx -17$ to –15) and low water content (~4.6 wt%), reflecting derivation from relatively less oxidized mantle-derived melts in an interoceanic arc setting. The Paleocene Gabral Quartz diorite formed at relatively shallow depths (2.8–3.4 kbar) with comparable redox conditions (–16 to –15) but with moderate water content (~5.8 wt%) reflecting limited oxidation despite modest enrichment in slab derived fluids. A significant transition occurred in the Early Eocene, marked by the crystallization of Deshai quartz diorite at greater depths (3.7–5.4 kbar) and elevated temperatures (751–799 °C), comparatively oxidized (–15 to –11) conditions, and high water content (~7.2 wt%) indicating significant interaction between oxidized slab fluids or crustal materials with mantle derived magmas. The post-collisional Mid-Eocene granitoids, emplaced at upper–mid crustal levels (2.7–4.9 kbar), retained oxidized states (–14 to –11), high water contents (7.7–6.3 wt%) coupled with high crystallization temperatures, marking the culmination of hot, hydrous magmatism during arc–continent collision. These interpretations are further supported by the Lu-Hf isotope values in the Cretaceous to Paleocene granitoids, which show increasingly super-chondritic compositions in Eocene plutons, consistent with significant slab fluid contributions and crustal assimilation, as inferred from the evolving thermal, redox, and hydration conditions (Fig. 13a).

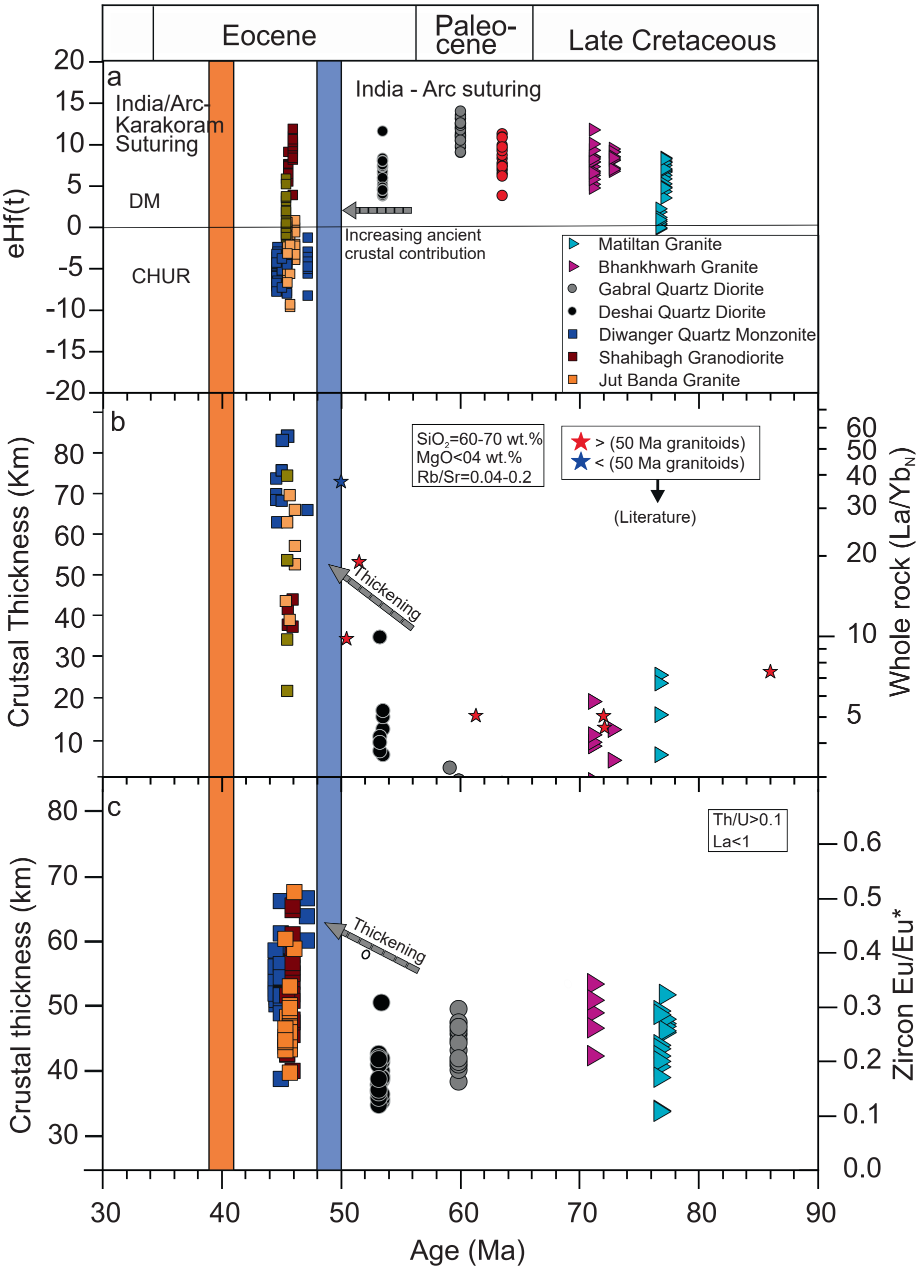

Fig. 13. Plots of zircon U-Pb ages a) versus zircon εHf(t) values (b) whole-rock $(La/Yb)_N$ ratios (crustal thickness), and (c) zircon Eu/Eu* (crustal thickness) of the granitoids from the central Kohistan arc. Whole rock geochemistry, ages and Hf data are from (Ahmad et al., 2025).

5.3. Tectonic implications and magma evolution

Zircon trace element chemistry, particularly U, Yb, and Nb concentrations, provides robust insights into magma sources, tectonic settings, and the degree of crustal contamination of granitoid magmas (Grimes et al., 2007). In the U/Yb vs. Hf and U vs. Yb diagrams (Fig. 12a, b), zircons from all granitoid plutons of the central KA plot within the continental crustal array, clearly separating them from oceanic crust zircons and confirming their continental affinity. Furthermore, all samples plot above the mantle array and within the magmatic arc field on the U/Yb vs. Nb/Yb diagram (Fig. 12c), highlighting the enrichment in fluid-mobile elements such as U relative to the fluid-immobile elements Yb and Nb, which is characteristic of subduction-related magmas.

Zircons from the arc-related Late Cretaceous Matiltan and Bhankhwarh granites, the Paleocene Gabral quartz diorite, and the Early Eocene Deshai quartz diorite display relatively low average U/Yb ratios (<1), consistent with values transitional between those of mid-ocean ridge basalts (MORB) and average continental crust (typically 0.1–1.0 (e.g., Carley et al., 2011, 2014). In contrast, zircons from the arc-continental collisional related Mid-Eocene plutons (Diwanger, Shahibagh, and Jut Banda) exhibit markedly elevated U/Yb ratios ranging from 1 to 10 (Fig. 12a, c). These higher values suggest increased contributions from mature, LIL-enriched continental crust during melt generation, consistent with enhanced crustal assimilation in collisional settings (Grimes et al., 2007). The elevated U/Yb ratios may also be partially attributed to crystal-melt partitioning behavior, as zircon preferentially incorporates Yb over U (Bea, 1996), leaving the residual melt enriched in U relative to Yb. Consequently, later-crystallizing zircon in more evolved magmas records higher U/Yb, particularly in Mid-Eocene collisional granitoids.

Additional constraints from Hf-Th-Nb systematics further support the arc-related origin of the granitoids. Zircons from all studied plutons fall within the orogenic field in Hf/Th vs. Th/Nb and Nb/Hf vs. Th/U

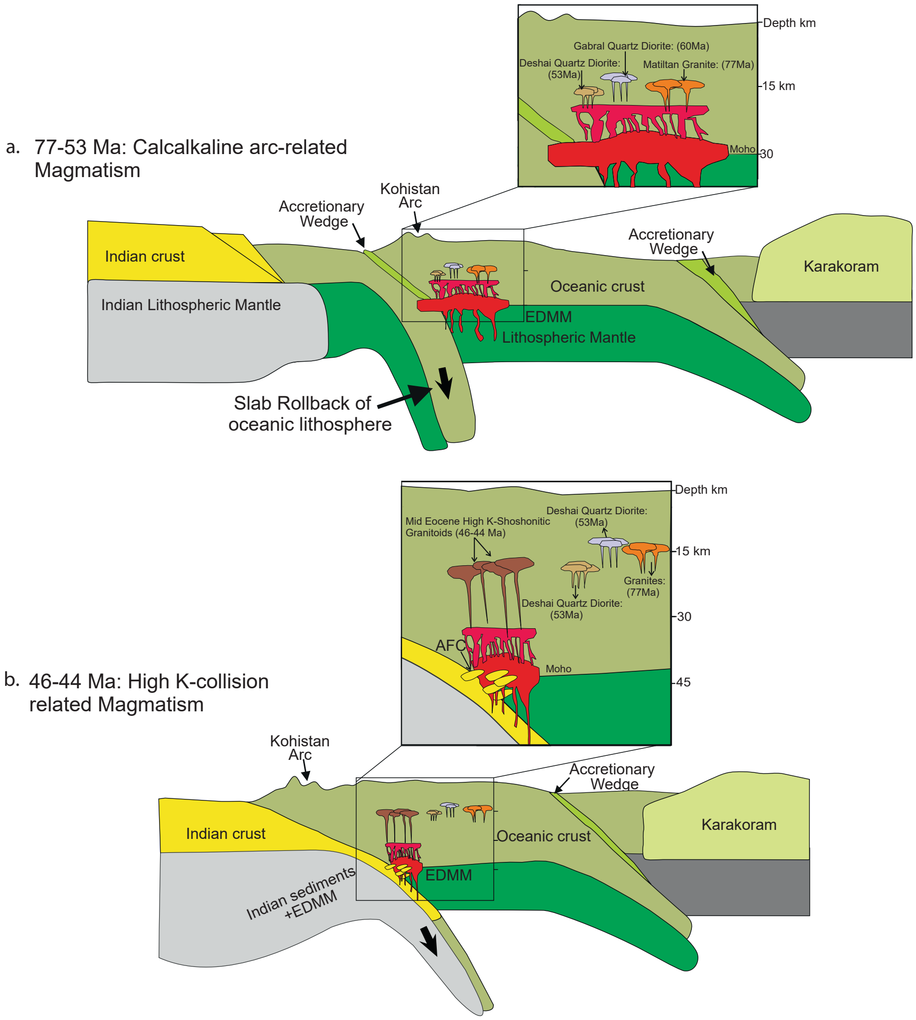

Fig. 14. Schematic tectonic evolution model representing two magmatic stages influenced by different tectonic settings. (a) Thin crust with production of Intra-arc subduction related calc-alkaline magmatism with limited crustal assimilation. (b) Thickened crust with high K- calc-alkaline magmatism influenced by variable stages of assimilation fractional crystallization (AFC).

diagrams (Fig. 12d, e), consistent with derivation from calc-alkaline arc magmas (Hawkesworth & Kemp, 2006). These geochemical patterns align with arc magmas that typically exhibit Nb depletion due to subduction-related processes, yielding low Nb/Hf and elevated Th/Nb ratios (Pearce & Peate, 1995; Sun & McDonough, 1989). However, a subset of zircons from the collisional Mid-Eocene granitoids, particularly from Diwanger, Shahibagh, and Jut Banda, plots near or outside the orogenic field, occasionally overlapping with the anorogenic domain (Fig. 12d). This geochemical deviation may reflect variable degrees of crustal assimilation, wherein the incorporation of continental material increased the Th/Nb ratios while reducing the Hf/Th ratios, thus shifting these samples away from typical arc signatures.

Biotite compositions, plotted in the ternary MgO-FeO$_t$-Al$_2$O$_3$ classification diagram of (Abdel. R 1994), also confirming the calc-alkaline orogenic nature of the studied granitoids (Fig. 5e). Collectively, zircon and biotite compositions strongly support an arc-related magmatic origin for most of the granitoids, with modifications in the Mid-Eocene plutons likely resulting from ancient crustal interaction due to India-Arc collision.

5.4. *Implications for crustal thickness evolution*

Zircon trace element data from central Kohistan Arc (KA) provide compelling evidence for significant crustal thickening during the Mid-Eocene, particularly between ca. 47–44 Ma. A pronounced increase in zircon Eu/Eu*, a reliable proxy for crustal thickness, is observed in the zircons of Mid-Eocene granitoids (Diwanger, Shahibagh, and Jut Banda), in contrast to the lower Eu/Eu* zircon values of the older Late Cretaceous to Early Eocene (77–53 Ma) granitoids such as the Matiltan, Bhankhwarh, Gabral, and Deshai plutons (Fig. 13c). These geochemical signatures reflect the changing tectonic setting and the increasing role of deep crustal processes during collisional magmatism (Fig. 14a and b).

Supporting evidence comes from the high La/Yb whole rock ratios of the Mid-Eocene granitoids (Ahmad et al., 2025b; Fig. 13b), which are indicative of partial melting in a garnet-bearing lower crust under high-pressure conditions. Such geochemical trends suggest (1) suppression of plagioclase crystallization in the magma and (2) presence of garnet in the source residue during partial melting, hallmarks of a thickened crustal column (Chapman et al., 2015; Hu et al., 2017; Profeta et al., 2015). This scenario promotes magmas with minimal Eu depletion and, moreover, leads to elevated Eu/Eu* values in crystallizing zircon. The pressure sensitivity of the Eu anomaly is rooted in the dual valence behavior of europium. At low pressures, typical of thin crust, plagioclase fractionation depletes Eu^{2+} from the magma, resulting in a pronounced negative Eu anomaly in zircon (Tang et al., 2024). In contrast, at higher pressures, typical of a thickened crust, plagioclase crystallization is suppressed, whereas garnet, amphibole, and clinopyroxene dominate the residual mineral assemblage. In such settings, garnet fractionation may also enhance melt oxidation (Tang et al., 2018), stabilizing Eu^{3+} over Eu^{2+}, which is more compatible with zircon and leads to higher Eu/Eu* values. This increase in zircon Eu/Eu* values in the investigated granitoid plutons during the Mid-Eocene marks a significant tectonic transition in the evolution of the KA.

This interpretation aligns with studies from other orogenic systems, particularly the Gangdese arc on the southern Tibetan Plateau, where elevated zircon Eu/Eu* has been directly linked to crustal thickening (Zhang et al., 2024). Tang et al., (2021) also demonstrated a correlation between Eu/Eu* in zircon and La/Yb in felsic melts, reflecting pressure-dependent mineral fractionation behavior and, thereby, serving as a reliable proxy for crustal thickness evolution during arc magmatism.

Two lines of evidence support the hypothesis that crustal thickening during this stage was primarily driven by continental collision, rather than arc-related mafic underplating: (1) Zircon εHf(t) values from the Mid-Eocene granitoids (Ahmad et al., 2025b) show enriched signatures, indicating the involvement of continental crust of the Indian craton in the magma source. This supports a model of crustal reworking and recycling, consistent with a collisional tectonic regime, and (2) The absence of coeval bimodal mafic intrusions, which are commonly associated with magmatic underplating in arc environments, also argues against arc-related thickening mechanisms.

In summary, the integrated evidence from zircon trace element chemistry, whole-rock geochemistry, amphibole-based pressure estimates, and the regional absence of mafic magmatism all converge to support a tectonic model in which continental collision, rather than subduction-driven arc magmatism, was the primary driver of crustal thickening and uplift in central KA during the Mid-Eocene (Fig. 14). This marks a pivotal phase in the tectonomagmatic evolution of the region, characterized by deeper magma storage, more oxidized and hydrous melts, and enhanced crustal assimilation during the Mid-Eocene.

6. Conclusions

1. Thermobarometry data provides new insights into the Cretaceous to mid-Tertiary magmatism of central KA, revealing a heterogeneous crustal architecture. Estimated crystallization temperatures and pressures for the Cretaceous to Paleocene granitoids range from 745 °C to 740 °C and 3.6 to 3.0 kbar, respectively. In contrast, Eocene granitoids show a broader range of T-P values of 774 °C to 785 °C and 4.5 to 3.6 kbar, indicating significant thermal variations and deeper plutonic emplacement during the Eocene magmatic evolution.
2. Oxygen fugacity and water contents of the granitoid magmas evolved systematically over time. The older Cretaceous to Paleocene plutons crystallized under relatively less oxidized conditions from less hydrous magmas, whereas the younger Eocene magmas were characterized by more oxidized and hydrous magma, reflecting a shift in magma composition during the arc-continent collisional modified source.
3. The zircon trace element composition consistently points to a continental arc tectonic setting for all Late Cretaceous to Eocene granitoids, indicating subduction-related magmatism. Mid-Eocene suites show evidence of deeper crustal processes being involved in the magma evolution and increased differentiation, with greater influence from slab-derived fluids and sediments during arc-continental collision.
4. Elevated zircon Eu/Eu ratios* in post-collisional Mid-Eocene granitoids (e.g., Diwanger, Shahibagh, and Jut Banda) imply significant crustal thickening, with estimated crustal thicknesses reaching approximately 50 km during this period. This interpretation is supported by high whole-rock La/Yb ratios, which are indicative of deep-seated garnet-bearing crustal source regions and are likely associated with the ongoing convergence between the Indian Plate and the Kohistan Arc.

CRediT authorship contribution statement

Tanveer Ahmad: Writing – original draft, Visualization, Validation, Software, Methodology, Investigation, Formal analysis, Conceptualization. **Kirsten Drüppel:** Writing – review & editing, Validation, Supervision, Methodology, Conceptualization. **M.Qasim Jan:** Writing – review & editing, Supervision, Methodology, Conceptualization. **Armin Zeh:** Writing – review & editing, Validation, Formal analysis. **Dominik C. Hezel:** Writing – review & editing, Validation, Methodology, Formal analysis.

Funding

This work was supported by Deutsche Forschungsgemeinschaft (DFG; Project no. DR 744/10–1) to K.D.

Declaration of competing interest

The authors declare that they have no known competing financial interests or personal relationships that could have appeared to influence the work reported in this paper.

Acknowledgments

We acknowledge the financial support of the Higher Education Commission (HEC) of Pakistan and Deutscher Akademischer Austauschdienst (DAAD) for the PhD fellowship to the first author. The Graduate School for Climate and Environment (GRACE), KIT, and the National Centre of Excellence in Geology, University of Peshawar, are thanked for funding the geological field trips. Dr. Matthias Schwotzer from the Institute of Functional Interfaces (IFG), KIT, is thanked for his assistance in producing the CL images. The authors express their gratitude to Kristian Nikoloski from AGW at KIT for thin section preparation, Vivien from Goethe University Frankfurt for her assistance during probe analysis and Abuzar Ghaffari, Umair Musawer, and Adeel Ahmad from NCEG, University of Peshawar, for their assistance during filed work at Kohistan Arc. M. Q. Jan acknowledges research grant from Pakistan Academy of Sciences (PAS RG103) and Research Fellowship of the Chinese Academy of Sciences (PIFI) for studies in northern Pakistan. We are thankful to Editors for editorial handling and two anonymous reviewers whose suggestions greatly enhanced the quality of the manuscript.

Appendix A. Supplementary data

Supplementary data to this article can be found online at https://doi.org/10.1016/j.jseaes.2026.107049.

Data availability

Data will be made available on request.

References

Abdel, R., 1994. Nature of biotites from alkaline, calc-alkaline, and peraluminous magmas. J. Petrol. 35, 525–541. https://doi.org/10.1093/petrology/35.2.525.

Ahmad, T., Jan, M.Q., Drüppel, K., 2025a. Geology of the central Kohistan Arc, Northern Swat, Kalam (NW, Pakistan), results of a new 1:50,000 scale geological mapping. J. Maps 21. https://doi.org/10.1080/17445647.2025.2572765.

Ahmad, T., Drüppel, K., Jan, M.Q., Zeh, A., Gerdes, A., 2025b. Tectono–magmatic evolution of the central Kohistan Magmatic Arc, pakistan—new constraints from zircon U–Pb dating, hf isotopes and geochemistry. J. Petrol. 66, egaf101. https://doi.org/10.1093/petrology/egaf101.

Ali, M., Zhao, K.D., Wang, C., Rehman, H.U., Hussain, A., Mahar, M.A., Farhan, M., Lutfi, W., 2024. Geochemical and isotopic constraints on the origin and evolution of the Matum-Das tonalite and mafic enclaves from the Kohistan Batholith, Northern Pakistan. Lithos 470, 107535. https://doi.org/10.1016/j.lithos.2024.

Anderson, J.L., Smith, D.R., 1995. The effects of temperature and fO_2 on the Al-in-hornblende barometer. Am. Mineral. 80, 549–559. https://doi.org/10.2138/am-1995-5-614.

Ballard, J.R., Palin, J.M., Campbell, I.H., 2002. Relative oxidation states of magmas inferred from Ce (IV)/Ce (III) in zircon: application to porphyry copper deposits of northern Chile. Contrib. Miner. Petrol. 144, 347–364. https://doi.org/10.1007/s00410-002-0402-5.

Barth, A.P., Wooden, J.L., 2010. Coupled elemental and isotopic analyses of polygenetic zircons from granitic rocks by ion microprobe, with implications for melt evolution and the sources of granitic magmas. Chem. Geol. 277, 149–159. https://doi.org/10.1016/j.chemgeo.2010.07.017.

Barth, A.P., Wooden, J.L., Jacobson, C.E., Economos, R.C., 2013. Detrital zircon as a proxy for tracking the magmatic arc system: the California arc example. Geology 41, 223–226. https://doi.org/10.1130/G33619.1.

Bea, F., 1996. Residence of REE, Y, Th and U in Granites and Crustal Protoliths; implications for the Chemistry of Crustal Melts. J. Petrol. 37, 521–552. https://doi.org/10.1093/petrology/37.3.521.

Belousova, E.A., Griffin, W.L., O'Reilly, S.Y., 2006. Zircon crystal morphology, trace element signatures and Hf isotope composition as a tool for petrogenetic modelling: examples from Eastern Australian granitoids. J. Petrol. 47, 329–353. https://doi.org/10.1093/petrology/egi077.

Belousova, E.A., Griffin, W.L., O'Reilly, S.Y., Fisher, N.I., 2002. Igneous zircon: trace element composition as an indicator of source rock type. Contrib. Miner. Petrol. 143, 602–622. https://doi.org/10.1007/s00410-002-0364-7.

Boehnke, P., Watson, E.B., Trail, D., Harrison, T.M., Schmitt, A.K., 2013. Zircon saturation re-revisited. Chem. Geol. 351, 324–334. https://doi.org/10.1016/j.chemgeo.2013.05.028.

Bouilhol, P., Jagoutz, O., Hanchar, J.M., Dudas, F.O., 2013. Dating the India-Eurasia collision through arc magmatic records. Earth Planet. Sci. Lett. 366, 163–175. https://doi.org/10.1016/j.epsl.2013.01.023.

Bouvier, A.-S., Ushikubo, T., Kita, N.T., Cavosie, A.J., Kozdon, R., Valley, J.W., 2012. Li isotopes and trace elements as a petrogenetic tracer in zircon: insights from Archean TTGs and sanukitoids. Contrib. Miner. Petrol. 163, 745–768. https://doi.org/10.1007/s00410-011-0697-1.

Burg, J.-P., Bouilhol, P., 2019. Timeline of the South Tibet – Himalayan belt: the geochronological record of subduction, collision, and underthrusting from zircon and monazite U–Pb ages. Can. J. Earth Sci. 56, 1318–1332. https://doi.org/10.1139/cjes-2018-0174.

Cao, Y., Li, S., Zhang, H., Liu, X., Li, Z., Ao, C., Yao, M., 2011. Significance of zircon trace element geochemistry, the Shihu gold deposit, western Hebei Province, North China. J. Rare Earths 29, 277–286. https://doi.org/10.1016/S1002-0721(10)60445-0.

Carley, T.L., Miller, C.F., Wooden, J.L., Bindeman, I.N., Barth, A.P., 2011. Zircon from historic eruptions in Iceland: Reconstructing storage and evolution of silicic magmas. Mineral. Petrol. 102, 135–161. https://doi.org/10.1007/s00710-011-0169-3.

Carley, T.L., Miller, C.F., Wooden, J.L., Padilla, A.J., Schmitt, A.K., Economos, R.C., Bindeman, I.N., Jordan, B.T., 2014. Iceland is not a magmatic analog for the Hadean: evidence from the zircon record. Earth Planet. Sci. Lett. 405, 85–97. https://doi.org/10.1016/j.epsl.2014.08.015.

Cavosie, A.J., Valley, J.W., Wilde, S.A., 2006. Correlated microanalysis of zircon: trace element, δ18O, and U-Th–Pb isotopic constraints on the igneous origin of complex >3900Ma detrital grains. Geochim. Cosmochim. Acta 70, 5601–5616. https://doi.org/10.1016/j.gca.2006.08.011.

Chapman, J.B., Ducea, M.N., DeCelles, P.G., Profeta, L., 2015. Tracking changes in crustal thickness during orogenic evolution with Sr/Y: an example from the north American Cordillera. Geology 43, 919–922. https://doi.org/10.1130/G36996.1.

Deer, W.A., Howie, R.A., Zussman, J., 2013. An introduction to the rock-forming minerals. Mineralogical Society of Great Britain and Ireland. https://doi.org/10.1180/DHZ.

Dhuime, B., Bosch, D., Garrido, C.J., Bodinier, J.L., Bruguier, O., Hussain, S.S., Dawood, H., 2009. Geochemical architecture of the lower- to middle-crustal section of a Paleo-island arc (Kohistan complex, Jijal-Kamila area, northern Pakistan): implications for the evolution of an oceanic subduction zone. J. Petrol. 50, 531–569. https://doi.org/10.1093/petrology/egp010.

El-Bialy, M.Z., Ali, K.A., 2013. Zircon trace element geochemical constraints on the evolution of the Ediacaran (600-614Ma) post-collisional Dokhan Volcanics and Younger Granites of SE Sinai, NE Arabian-Nubian Shield. Chem. Geol. 360–361, 54–73. https://doi.org/10.1016/j.chemgeo.2013.10.009.

Erdmann, S., Martel, C., Pichavant, M., Kushnir, A., 2014. Amphibole as an archivist of magmatic crystallization conditions: problems, potential, and implications for inferring magma storage prior to the paroxysmal 2010 eruption of Mount Merapi, Indonesia. Contrib. Miner. Petrol. 167, 1016. https://doi.org/10.1007/s00410-014-1016-4.

Ferry, J.M., Watson, E.B., 2007. New thermodynamic models and revised calibrations for the Ti-in-zircon and Zr-in-rutile thermometers. Contrib. Miner. Petrol. 154, 429–437. https://doi.org/10.1007/s00410-007-0201-0.

Foster, M. D., 1960. *Interpretation of the composition of trioctahedral micas*. Geological Survey Professional paper, 354. United States government printing office, Washington. Doi: 10.3133/pp354B.

Fu, B., Mernagh, T.P., Kita, N.T., Kemp, A.I.S., Valley, J.W., 2009. Distinguishing magmatic zircon from hydrothermal zircon: a case study from the Gidginbung high-sulphidation Au–Ag–(Cu) deposit, SE Australia. Chem. Geol. 259, 131–142. https://doi.org/10.1016/j.chemgeo.2008.10.035.

Geisler, T., Rashwan, A.A., Rahn, M.K.W., Poller, U., Zwingmann, H., Pidgeon, R.T., Schleicher, H., Tomaschek, F., 2003. Low-temperature hydrothermal alteration of natural metamict zircons from the Eastern Desert, Egypt. Mineral. Mag. 67, 485–508. https://doi.org/10.1180/0026461036730112.

Grimes, C.B., John, B.E., Kelemen, P.B., Mazdab, F.K., Wooden, J.L., Cheadle, M.J., Hanghøj, K., Schwartz, J.J., 2007. Trace element chemistry of zircons from oceanic crust: a method for distinguishing detrital zircon provenance. Geology 35, 643–646. https://doi.org/10.1130/G23603A.1.

Grimes, C.B., Wooden, J.L., Cheadle, M.J., John, B.E., 2015. Fingerprinting" tectono-magmatic provenance using trace elements in igneous zircon. Contributions to Mineralogy and Petrology 170, 46.

Harrison, T.M., Schmitt, A.K., McCulloch, M.T., Lovera, O.M., 2008. Early (≥4.5 Ga) formation of terrestrial crust: Lu–Hf, δ18O, and Ti thermometry results for Hadean zircons. Earth Planet. Sci. Lett. 268, 476–486. https://doi.org/10.1016/j.epsl.2008.02.011.

Hawkesworth, C.J., Kemp, A.I.S., 2006. Using hafnium and oxygen isotopes in zircons to unravel the record of crustal evolution. Chem. Geol. 226, 144–162. https://doi.org/10.1016/j.chemgeo.2005.09.018.

Hawthorne, F.C., Oberti, R., Harlow, G.E., Maresch, W.V., Martin, R.F., Schumacher, J. C., Welch, M.D., 2012. IMA report: Nomenclature of the amphibole supergroup. Am. Mineral. 97, 2031–2048. https://doi.org/10.2138/am.2012.4276.

Henry, D.J., 2005. The Ti-saturation surface for low-to-medium pressure metapelitic biotites: implications for geothermometry and Ti-substitution mechanisms. Am. Mineral. 90, 316–328. https://doi.org/10.2138/am.2005.1498.

Heuberger, S., Schaltegger, U., Burg, J.P., Villa, I.M., Frank, M., Dawood, H., Hussain, S., Zanchi, A., 2007. Age and isotopic constraints on magmatism along the Karakoram-Kohistan Suture Zone, NW Pakistan: evidence for subduction and continued convergence after India-Asia collision. Swiss J. Geosci. 100, 85–107. https://doi.org/10.1007/s00015-007-1203-7.

Hidaka, H., Shimizu, H., Adachi, M., 2002. U–Pb geochronology and REE geochemistry of zircons from Palaeoproterozoic paragneiss clasts in the Mesozoic Kamiaso conglomerate, central Japan: evidence for an Archean provenance. Chem. Geol. 187, 279–293. https://doi.org/10.1016/S0009-2541(02)00058-X.

Hinton, R.W., Upton, B.G.J., 1991. The chemistry of zircon: variations within and between large crystals from syenite and alkali basalt xenoliths. Geochim. Cosmochim. Acta 55, 3287–3302. https://doi.org/10.1016/0016-7037(91)90489-R.

Hirschmann, M.M., Ghiorso, M.S., Davis, F.A., Gordon, S.M., Mukherjee, S., Grove, T.L., Till, C.B., 2008. Library of Experimental Phase Relations (LEPR): A database and Web portal for experimental magmatic phase equilibria data. Geochemistry, Geophysics, Geosystems 9, 3.

Holland, T., Blundy, J., 1994. Non-ideal interactions in calcic amphiboles and their bearing on amphibole-plagioclase thermometry. Contrib. Miner. Petrol. 116, 433–447. https://doi.org/10.1007/BF00310910.

Hoskin, P.W.O., 2005. Trace-element composition of hydrothermal zircon and the alteration of Hadean zircon from the Jack Hills, Australia. Geochim. Cosmochim. Acta 69, 637–648. https://doi.org/10.1016/j.gca.2004.07.006.

Hoskin, P.W.O., Ireland, T.R., 2000. Rare earth element chemistry of zircon and its use as a provenance indicator. Geology 28, 627. https://doi.org/10.1130/0091-7613(2000)28<627.

Hoskin, P.W.O., Kinny, P.D., Wyborn, D., Chappell, B.W., 2000. Identifying accessory mineral saturation during differentiation in granitoid magmas: an integrated approach. In Journal of Petrology 41, 1365–1396. https://doi.org/10.1093/petrology/41.9.1365.

Hoskin, P.W., Schaltegger, U., 2003. The composition of zircon and igneous and metamorphic petrogenesis. Reviews in mineralogy and geochemistry 53, 27–62.

Hu, F., Ducea, M.N., Liu, S., Chapman, J.B., 2017. Quantifying crustal thickness in continental collisional belts: global perspective and a geologic application. Sci. Rep. 7, 7058. https://doi.org/10.1038/s41598-017-07849-7.

Pupin, J.P., 1980. Zircon and granite petrology. Contribution to Minerology and Petrology 73, 207–220. https://doi.org/10.1007/BF00381441.

Jagoutz, O., Bouilhol, P., Schaltegger, U. R. S., Müntener, O., 2018. The isotopic evolution of the Kohistan Ladakh arc from subduction initiation to continent arc collision. In *Geological Society Special Publication* 483, 165–182. Geological Society of London. Doi: 10.1144/SP483.7.

Jagoutz, O., Burg, J.P., Hussain, S., Dawood, H., Pettke, T., Iizuka, T., Maruyama, S., 2009. Construction of the granitoid crust of an island arc part I: geochronological and geochemical constraints from the plutonic Kohistan (NW Pakistan). Contrib. Miner. Petrol. 158, 739–755. https://doi.org/10.1007/s00410-009-0408-3.

Jagoutz, O., Schmidt, M.W., 2012. The formation and bulk composition of modern juvenile continental crust: the Kohistan arc. Chem. Geol. 298–299, 79–96. https://doi.org/10.1016/j.chemgeo.2011.10.022.

Jan, M.Q., Asif, M., 1983. Geochemistry of tonalites and (quartz) diorites of the Kohistan-Ladakh (Trans Himalayan) granitic belt in Swat, NW Pakistan. In: Granites of Himalaya, Karakoram and Hindukush. Punjab Univ. Lahore, Geology, pp. 355–376.

Jan, M.Q., Howie, R.A., 1981. The mineralogy and geochemistry of the metamorphosed basic and ultrabasic rocks of the Jijal complex, Kohistan, NW Pakistan. Journal of Petrology 22, 85–126.

Jan, M.Q., Mian, I., 1971. Prelimanary geology and petrography of swat kohistan. Journal of Himalayan Earth Sciences 6, 1–32.

Johnson, K.T.M., 1998. Experimental determination of partition coefficients for rare earth and high-field-strength elements between clinopyroxene, garnet, and basaltic melt at high pressures. Contrib. Miner. Petrol. 133, 60–68. https://doi.org/10.1007/s004100050437.

Kazmi, A.H., Jan, M.Q., 1997. Geology & Tectonics of Pakistan. GraphicPublisher Karachi, Pakistan,.554.

Khalil, M.A., Afridi, A.G.K., 1979. The geology and petrography of deshai-diwangar area, Ushu Gol valley, Swat Kohistan. Journal of Himalayan Earth Sciences 11, 99–111.

Khan, M.A., Jan, M.Q., Weaver, B.L., 1993. Evolution of the lower arc crust in Kohistan, N. Pakistan: temporal arc magmatism through early, mature and intra-arc rift stages.

Geol. Soc. Lond. Spec. Publ. 74, 123–138. https://doi.org/10.1144/GSL.SP.1993.074.01.10.

Khan, T., Jan, M.Q., Khan, M.A., Kausar, A.B., 1997. High-grade metasedimentary rocks (Gilgit Formation) in the vicinity of Gilgit, Kohistan, northern Pakistan. Journal of Minerology, Petrology and Economic Geology 92, 465–479. https://doi.org/10.2465/ganko.92.465.

Liu, Y., Hu, Z., Zong, K., Gao, C., Gao, S., Xu, J., Chen, H., 2010. Reappraisement and refinement of zircon U-Pb isotope and trace element analyses by LA-ICP-MS. Chin. Sci. Bull. 55, 1535–1546. https://doi.org/10.1007/s11434-010-3052-4.

Mutch, E.J.F., Blundy, J.D., Tattitch, B.C., Cooper, F.J., Brooker, R.A., 2016. An experimental study of amphibole stability in low-pressure granitic magmas and a revised Al-in-hornblende geobarometer. Contrib. Miner. Petrol. 171, 85. https://doi.org/10.1007/s00410-016-1298-9.

Nachit, H., Ibhi, A., Abia, E.H., Ben Ohoud, M., 2005. Discrimination between primary magmatic biotites, reequilibrated biotites and neoformed biotites. Comptes Rendus. Géoscience 337, 1415–1420. https://doi.org/10.1016/j.crte.2005.09.002.

Orejana, D., Villaseca, C., Armstrong, R.A., Jeffries, T.E., 2011. Geochronology and trace element chemistry of zircon and garnet from granulite xenoliths: constraints on the tectonothermal evolution of the lower crust under central Spain. Lithos 124, 103–116. https://doi.org/10.1016/j.lithos.2010.10.011.

Orejana, D., Villaseca, C., Valverde-Vaquero, P., Belousova, E.A., Armstrong, R.A., 2012. U–Pb geochronology and zircon composition of late Variscan S- and I-type granitoids from the Spanish Central System batholith. Int. J. Earth Sci. 101, 1789–1815. https://doi.org/10.1007/s00531-012-0750-y.

Pearce, J.A., Peate, D.W., 1995. Tectonic implications of the composition of volcanic ARC magmas. Annu. Rev. Earth Planet. Sci. 23, 251–285. https://doi.org/10.1146/annurev.ea.23.050195.001343.

Petterson, M.G., 2010. A review of the geology and tectonics of the Kohistan island arc, north Pakistan. Geological Society London Special Publication 338, 287–327. https://doi.org/10.1144/SP338.14.

Petterson, M.G., 2019. The plutonic crust of Kohistan and volcanic crust of Kohistan–Ladakh, North Pakistan/India: lessons learned for deep and shallow arc processes. In Geological Society London Special Publication 483, 123–164. https://doi.org/10.1144/SP483.4.

Petterson, M.G., Windley, B.F., 1985. Rb-Sr dating of the Kohistan arc-batholith in the Trans-Himalaya of north Pakistan, and tectonic implications. Earth Planet. Sci. Lett. 74, 45–57. https://doi.org/10.1016/0012-821X (85)90165-7.

Petterson, M.G., Windley, B.F., 1991. *Changing source regions of magmas and crustal growth in the Trans-Himalayas-evidence from the Chalt volcanics and Kohistan batholith, Kohistan, northern Pakistan.* Earth Planet. Sci. Lett. 102, 326–341. https://doi.org/10.1016/0012-821X(91)90027-F.

Pettke, T., Audétat, A., Schaltegger, U., Heinrich, C.A., 2005. Magmatic-to-hydrothermal crystallization in the W–Sn mineralized Mole Granite (NSW, Australia). Chem. Geol. 220, 191–213. https://doi.org/10.1016/j.chemgeo.2005.02.017.

Philpotts, J.A., 1970. Redox estimation from a calculation of Eu^{2+} and Eu^{3+} concentrations in natural phases. Earth Planet. Sci. Lett. 9, 257–268. https://doi.org/10.1016/0012-821X(70)90036-1.

Profeta, L., Ducea, M.N., Chapman, J.B., Paterson, S.R., Gonzales, S.M.H., Kirsch, M., Petrescu, L., DeCelles, P.G., 2015. Quantifying crustal thickness over time in magmatic arcs. Sci. Rep. 5, 17786. https://doi.org/10.1038/srep17786.

Pudsey, C.J., Coward, M.P., Luff, I.W., Shackleton, R.M., Windley, B.F., Jan, M.Q., 1985. Collision zone between the Kohistan arc and the asian plate in NW Pakistan. Transactions of the Royal Society of Edinburgh 76, 463–479. https://doi.org/10.1017/S026359330001066X.

Pupin, J.P., 2024. Zircon typology: a synthesis. applications to magmatic, metamorphic and sedimentary rocks. J. Petrol. 65, egae111. https://doi.org/10.1093/petrology/egae111.

Putirka, K., 2016. Amphibole thermometers and barometers for igneous systems and some implications for eruption mechanisms of felsic magmas at arc volcanoes. Am. Mineral. 101, 841–858. https://doi.org/10.2138/am-2016-5506.

Putirka, K.D., 2005. Igneous thermometers and barometers based on plagioclase + liquid equilibria: tests of some existing models and new calibrations. Am. Mineral. 90, 336–346. https://doi.org/10.2138/am.2005.1449.

Wones, D.R., 1989. Significance of the assemblage titanite+ magnetite+ quartz in granitic rocks. American Mineralogist 74, 744–749.

Wones David, R., Eugster Hans, P., 1965. Stability of biotite: experiment, theory, and application. Am. Mineral. 50, 1228–1272.

Ridolfi, F., 2021. Amp-tb2: an updated model for calcic amphibole thermobarometry. Minerals 11, 1–9. https://doi.org/10.3390/min11030324.

Ridolfi, F., Renzulli, A., 2012. Calcic amphiboles in calc-alkaline and alkaline magmas: thermobarometric and chemometric empirical equations valid up to 1,130°C and 2.2 GPa. Contrib. Miner. Petrol. 163, 877–895. https://doi.org/10.1007/s00410-011-0704-6.

Ridolfi, F., Renzulli, A., Puerini, M., 2010. Stability and chemical equilibrium of amphibole in calc-alkaline magmas: an overview, new thermobarometric formulations and application to subduction-related volcanoes. Contrib. Miner. Petrol. 160, 45–66. https://doi.org/10.1007/s00410-009-0465-7.

Schaltegger, U., Zeilinger, G., Frank, M., Burg, J., 2002. Multiple mantle sources during island arc magmatism: U–Pb and Hf isotopic evidence from the Kohistan arc complex, Pakistan. Terra Nova 14, 461–468. https://doi.org/10.1046/j.1365-3121.2002.00432.

Schmidt, M.W., 1992. Amphibole composition in tonalite as a function of pressure: an experimental calibration of the Al-in-hornblende barometer. Contrib. Miner. Petrol. 110, 304–310. https://doi.org/10.1007/BF00310745.

Searle, M.P., Khan, M.A., Fraser, J.E., Gough, S.J., Jan, M.Q., 1999. The tectonic evolution of the Kohistan-Karakoram collision belt along the Karakoram Highway transects, North Pakistan. Tectonics 18, 929–949. https://doi.org/10.1029/1999TC900042.

Searle, M.P., Windley, B.F., Coward, M.P., Cooper, D.J.W., Rex, A.J., Rex, D., Tingdong, L., Xuchang, X., Jan, M.Q., Thakur, V.C., Kumar, S., 1987. The closing of Tethys and the tectonics of the Himalaya. Geol. Soc. Am. Bull. 98, 678–701. https://doi.org/10.1130/0016-7606(1987)98.

Sun, S., McDonough, W.F., 1989. Chemical and isotopic systematics of oceanic basalts: implications for mantle composition and processes. Geol. Soc. Lond. Spec. Publ. 42, 313–345. https://doi.org/10.1144/GSL.SP.1989.042.01.19.

Symes, R.F., Bevan, J.C., Qasim Jan, M., 1987. The nature and origin of orbicular rocks from near Deshai, Swat Kohistan, Pakistan. Mineral. Mag. 51, 635–647. https://doi.org/10.1180/minmag.1987.051.363.02.

Tahirkheli, R.A.K., Jan, M.Q., 1979. Geology of Kohistan, Karakoram, Himalaya, northern Pakistan. Journal of Himalayan Earth Sciences 11, 1–187.

Tang, M., Erdman, M., Eldridge, G., Lee, C.-T.-A., 2018. The redox "filter" beneath magmatic orogens and the formation of continental crust. Sci. Adv. 4, aar4444. https://doi.org/10.1126/sciadv.

Tang, M., Guo, Z., Cao, W., Chu, X., 2024a. Revisiting zircon Eu anomaly as a proxy for crustal thickness: a case study of the Sierra Nevada Batholith. Earth Planet. Sci. Lett. 643, 118897. https://doi.org/10.1016/j.epsl.2024.

Tang, M., Ji, W.Q., Chu, X., Wu, A., Chen, C., 2021. Reconstructing crustal thickness evolution from europium anomalies in detrital zircons. Geology 49, 76–80. https://doi.org/10.1130/G47745.1.

Tang, W.L., Huang, F., Xu, J.F., Zeng, Y.C., Liu, X.J., 2024b. Cretaceous magmatism in the northern Lhasa Terrane: Implications for the tectonic evolution and crustal growth tempos of central Tibet. Bull. Geol. Soc. Am. 136, 3440–3456. https://doi.org/10.1130/B36986.1.

Tischendorf, G., Gottesmann, B., Förster, H.-J., Trumbull, R.B., 1997. On Li-bearing micas: estimating Li from electron microprobe analyses and an improved diagram for graphical representation. Mineral. Mag. 61, 809–834. https://doi.org/10.1180/minmag.1997.061.409.05.

Trail, D., Bruce Watson, E., Tailby, N.D., 2012. Ce and Eu anomalies in zircon as proxies for the oxidation state of magmas. Geochim. Cosmochim. Acta 97, 70–87. https://doi.org/10.1016/j.gca.2012.08.032.

Treloar, P.J., Petterson, M.G., Jan, M.Q., Sullivan, M.A., 1996. A re-evaluation of the stratigraphy and evolution of the Kohistan arc sequence, Pakistan Himalaya: implications for magmatic and tectonic arc-building processes. J. Geol. Soc. London 153, 681–693. https://doi.org/10.1144/gsjgs.153.5.0681.

Ullah, M., Klötzli, U., Rentenberger, C., Sláma, J., Younas, M., Khubab, M., Goudarzi, M., Ahmad, T., 2025. Unravelling the geochemical and geochronological diversities of the pre-collisional magmatism: Implications for the subduction dynamics in the Kohistan island arc and Karakorum block, Pakistan. Geosci. Front. 16, 102003. https://doi.org/10.1016/j.gsf.2025.102003.

Van Lichtervelde, M., Holtz, F., Dziony, W., Ludwig, T., Meyer, H.-P., 2011. Incorporation mechanisms of Ta and Nb in zircon and implications for pegmatitic systems. Am. Mineral. 96, 1079–1089. https://doi.org/10.2138/am.2011.3650.

Wang, W., Liu, S., Bai, X., Li, Q., Yang, P., Zhao, Y., Zhang, S., Guo, R., 2013. Geochemistry and zircon U–Pb–Hf isotopes of the late Paleoproterozoic Jianping diorite–monzonite–syenite suite of the North China Craton: implications for petrogenesis and geodynamic setting. Lithos 162, 175–194. https://doi.org/10.1016/j.lithos.2013.01.005.

Watson, E.B., Harrison, T.M., 1983. Zircon saturation revisited' temperature and composition effects in a variety of crustal magma types. In Earth and Planetary Science Letters. 64, 295–304. https://doi.org/10.1016/0012-821X(83)90211-X.

Xia, Q.-X., Zheng, Y.-F., Hu, Z., 2010. Trace elements in zircon and coexisting minerals from low-T/UHP metagranite in the Dabie orogen: Implications for action of supercritical fluid during continental subduction-zone metamorphism. Lithos 114, 385–412. https://doi.org/10.1016/j.lithos.2009.09.013.

Yang, J., Cawood, P.A., Du, Y., Huang, H., Huang, H., Tao, P., 2012. Large Igneous Province and magmatic arc sourced Permian–Triassic volcanogenic sediments in China. Sedimentary Geology 261, 120–131.

Zhang, Z.M., Ding, H.X., Palin, R.M., Dong, X., Tian, Z.L., Li, X.W., 2024. Crustal evolution of a continental magmatic arc from subduction to collision: a case study in the Gangdese arc, southern Tibetan Plateau. Bull. Geol. Soc. Am. 136, 4059–4071. https://doi.org/10.1130/B37171.1.

Zhong, S., Feng, C., Seltmann, R., Li, D., Qu, H., 2018. Can magmatic zircon be distinguished from hydrothermal zircon by trace element composition? the effect of mineral inclusions on zircon trace element composition. Lithos 314, 646–657. https://doi.org/10.1016/j.lithos.2018.06.029.